

# Effect of Flow-Duct Geometry on Solid Desiccant Dehumidification

Hassan S. Al-Sharqawi

Medina College of Technology, Department of Mechanical Technology, P.O. Box 1593, Medina, Saudi Arabia

Noam Lior\*

University of Pennsylvania, Department of Mechanical Engineering and Applied Mechanics, Philadelphia, Pennsylvania 19104-6315

This study presents a comparative numerical solution of a conjugate-transient three-dimensional heat and mass transfer problem between a solid desiccant (silica gel) and a humid transient-laminar air stream in ducts with different cross-sectional geometries: square, circular, and triangular. The problem is solved by using a finite control-volume method and validated relative to available experimental data. The effects of the  $u$  velocity gradient normal to the wall ( $\partial u/\partial y$ ) and the pressure drop ( $\Delta p$ ) on the heat and mass transport for the three ducts are investigated. In duct flows, the results show that the average ( $\partial u/\partial y$ ) for the triangular duct is 6.6% and 19.6% larger than that in the circular and square ducts, respectively; therefore, the triangular duct provides the largest convective heat and mass transport and absorbs 11% and 42% more water than the circular and square ducts, respectively. At the same time, the average pressure drop for the triangular duct is 69% and 73.5% larger than that for the square and circular ducts, respectively, which would result in higher fan power consumption. Using a figure of merit ( $W_r$ ) that is a ratio of the required fan work to the dehumidification attained, the circular duct was found to be the best and the triangular duct was found to be the worst among the three geometries compared. The results obtained from this study can also be useful for designing desiccant ducts, as they give guidance about duct length optimization and duct cross-sectional shape considering both dehumidification effectiveness and flow pressure drop.

## 1. Introduction

The general objective of this study is to develop more rigorous models of solid bed desiccant channel systems used for gas dehumidification, as well as to solve and analyze them specifically for different desiccant-lined channel geometries. This should improve the basic understanding of the process and, thus, of ways for improving overall performance of such systems. Beside the contribution to the fundamental understanding of these physicochemical processes, the results are intended to help design flow dehumidification desiccant channels that could then be optimized for most effective dehumidification and lowest pressure drop and cost.

One of the main initial past studies of a similar problem is the one by Fujii and Lior,<sup>1</sup> who solved numerically the conjugate-transient two-dimensional heat and mass transfer problem with a steady laminar air stream passing over a thick silica gel bed. More recently, Al-Sharqawi and Lior<sup>2</sup> developed and solved a conjugate-transient two-dimensional flow and heat and mass transfer model of humid laminar and turbulent air flow fields over desiccant-lined finite flat plates and inside parallel-plate channels. Niu and Zhang<sup>3</sup> solved numerically the conjugate-transient two-dimensional heat and mass transfer in a laminar flow silica gel-lined channel, which is a cell in a desiccant wheel, to investigate the effects of the channel wall thickness on the optimal rotary speed of such wheels. They considered both the heat and the moisture resistance in both the axial and thickness directions in the silica gel to simulate the heat and mass transfers in a desiccant wheel. Niu and Zhang<sup>4</sup> also studied numerically the thermally developing laminar forced-convection flow and heat transfer characteristics in corrugated ducts confined by sinusoidal and arc curves that shape a honeycomb rotary wheel heat exchanger.

Slightly related problems of flow and transport in porous channels treated recently are described in the following. Haji-Sheikh and Vafai<sup>5</sup> investigated mathematically the heat transfer to a fully developed flow passing through a channel filled with porous materials (no free flow). Their investigation included the derivation of the temperature solutions in channels having different cross-sectional geometries, namely, parallel-plate channels, circular tubes, and elliptical passages. This problem is different from the one we are treating. Haji-Sheikh<sup>6</sup> investigated theoretically and numerically the fully developed forced convection heat transfer to fluid flow in various rectangular ducts filled with porous materials and with classical boundary conditions. He assumed that the Brinkman model for unidirectional flow in a duct represents the velocity field for a specified porous passage. An exact series solution was achievable for a rectangular duct, too. Hooman et al.<sup>7</sup> studied analytically the heat transfer to fully developed forced convection flow inside a rectangular duct filled with a porous-saturated material. They presented a sensitivity analysis of the Nusselt number, Bejan number, and dimensionless entropy generation rate to the system parameters, particularly to optimize alternative rectangular duct design options in terms of heat transfer, pressure drop, and entropy generation.

In this paper, we address a transient-laminar air stream passing inside square, circular, and triangular flow cross section ducts lined internally with 3 mm thick desiccant beds, at free stream Reynolds number of 666 for the square and circular ducts and 420 for the triangular duct. Dehumidification in desiccant-lined ducts is common in desiccant wheels, and the flow geometries considered here were selected for the examination of some limiting cases but do not consider rotation of the channel. The model includes heat conduction and mass diffusion inside the desiccant bed. The numerical solution is one of a conjugate-transient three-dimensional heat and mass transfer problem

\* To whom correspondence should be addressed. E-mail: lior@seas.upenn.edu.

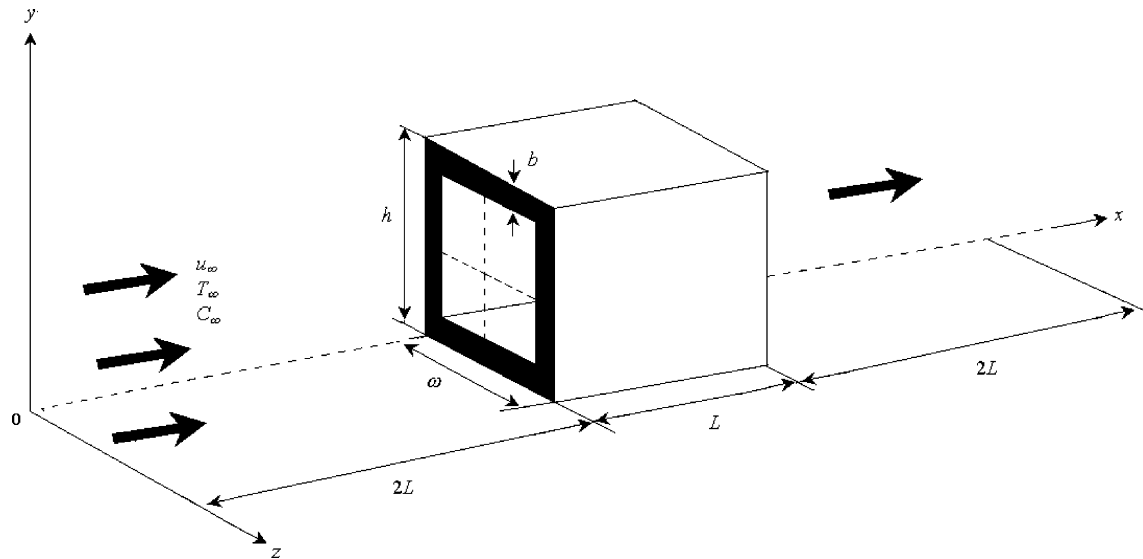


Figure 1. Square duct with extended computational domain along the  $x$ -direction.

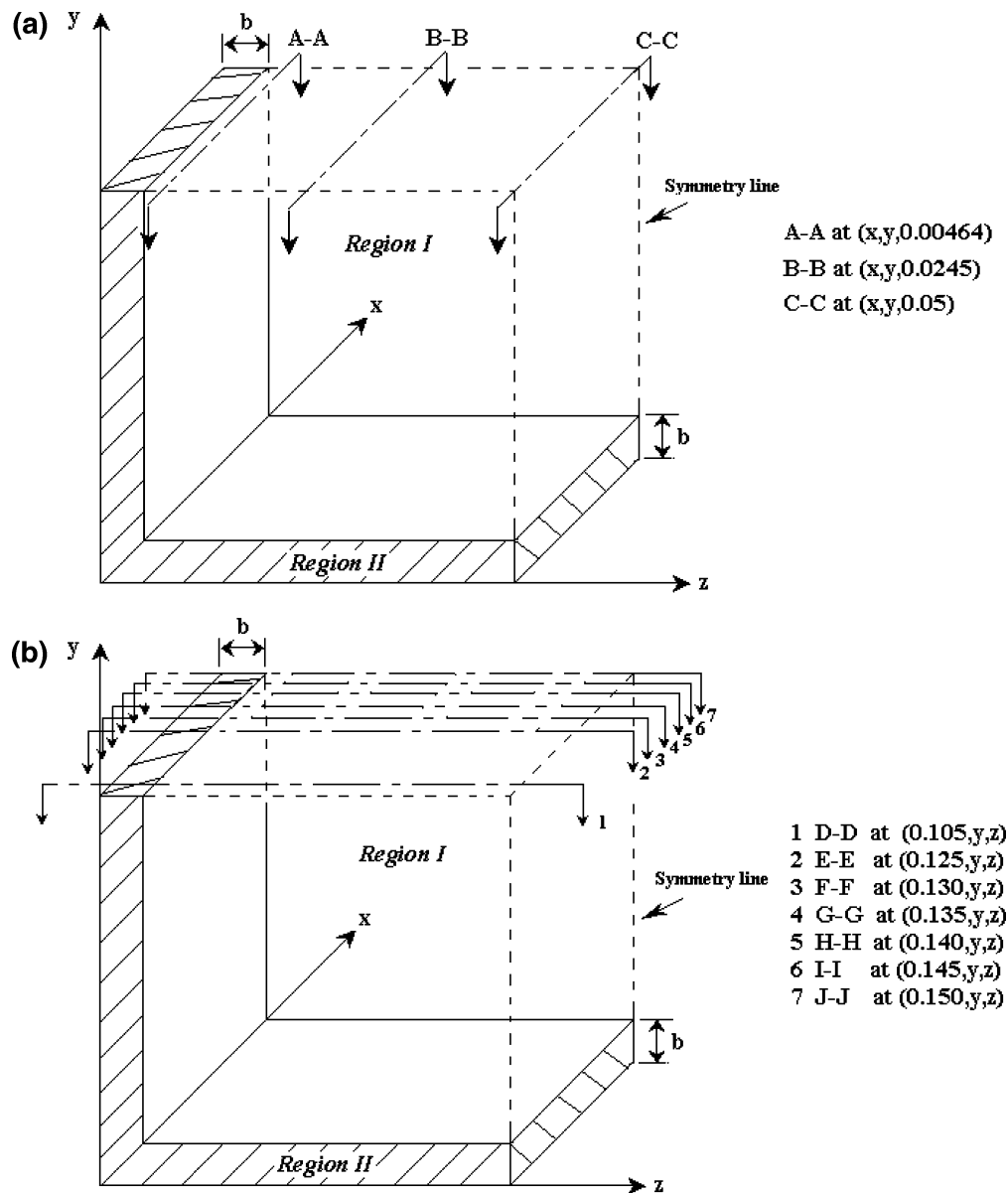
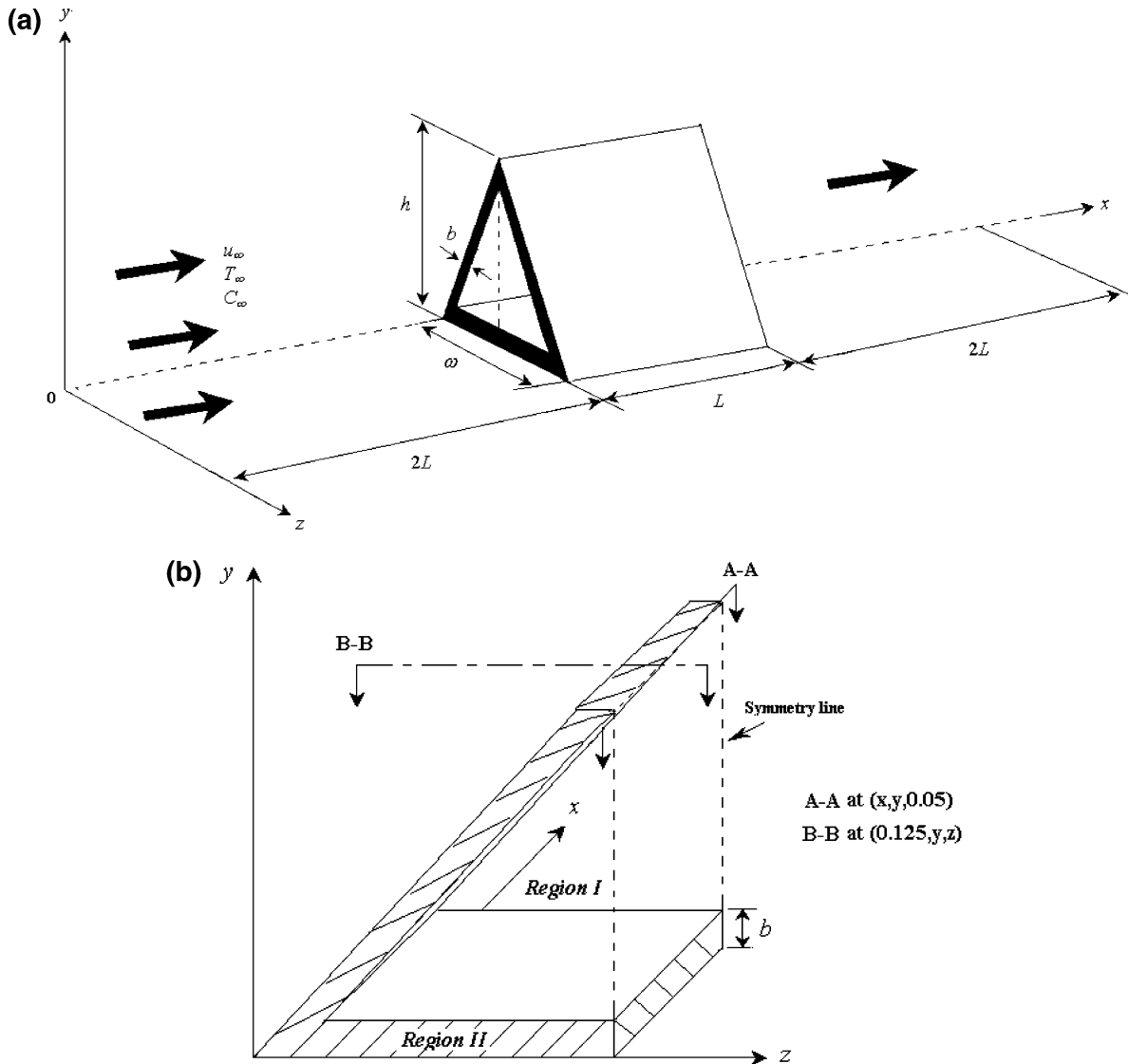


Figure 2. One-quarter of the square duct with different cross-sectional areas: (a) along  $z$ -axis and (b) along  $x$ -axis.



**Figure 3.** Triangular duct with (a) extended computational domain along the  $x$ -direction and (b) with two cross-sectional areas along the  $z$ -axis (one-half of triangular duct).

between the solid desiccant (silica gel) and a humid laminar air stream in the ducts.

## 2. Model Configuration

Figure 1 shows the extended computational domain of the square duct along the  $x$ -direction (flow), where  $h$  is the overall height in the  $y$ -direction,  $\omega$  is the overall width in the  $z$ -direction,  $L$  is the duct length in the  $x$ -direction, and  $b$  is the desiccant bed thickness. One-quarter of the duct structure is used in the computational process because of the duct's symmetry, as shown in Figure 2. Parts a and b of Figure 2 present schematic diagrams of the cross-sectional planes along the  $z$ - and  $x$ -axes, respectively, at which computed data are presented.

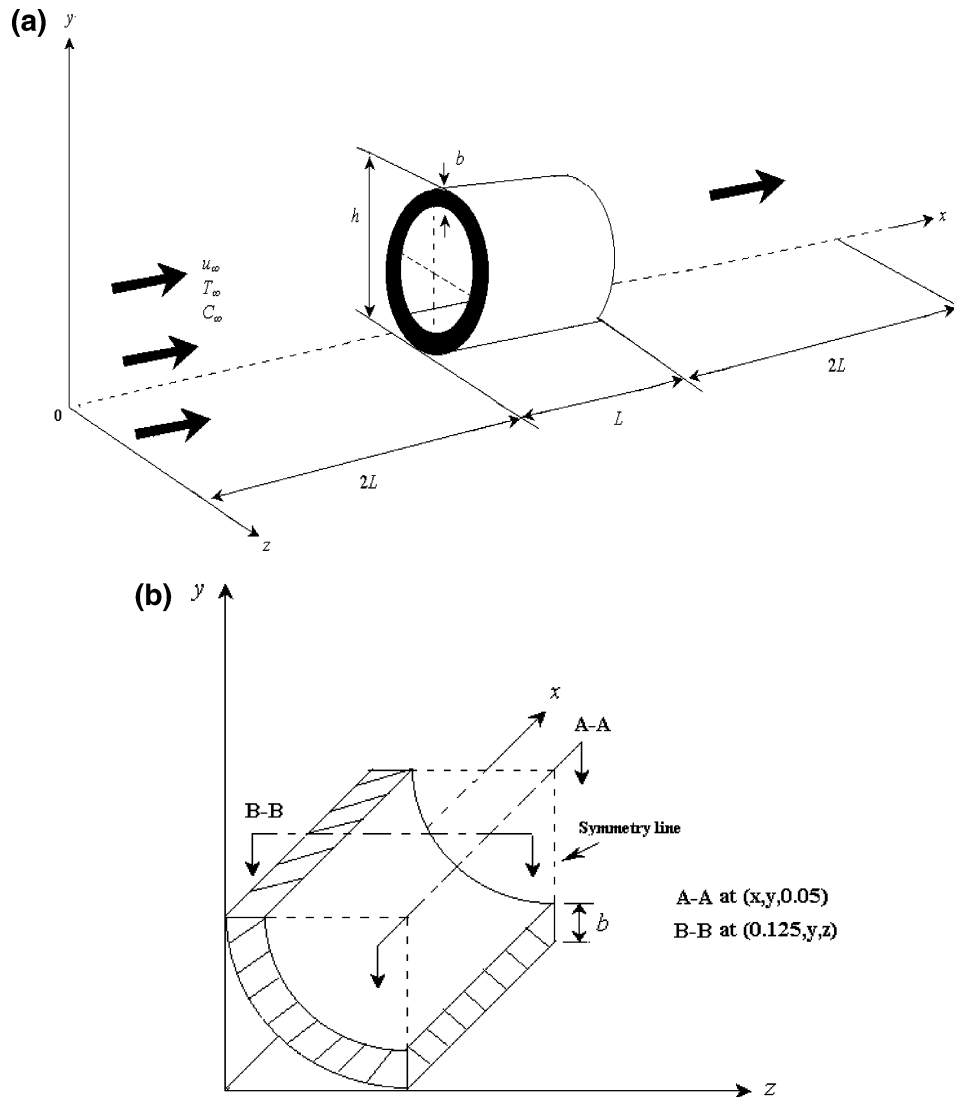
Figure 3a shows the extended computational domain of the triangular duct along the  $x$ -direction (flow), where  $h$  is the overall height in the  $y$ -direction,  $\omega$  is the overall width in the  $z$ -direction,  $L$  is the duct length in the  $x$ -direction, and  $b$  is the desiccant bed thickness. One-half of the duct structure is used in the computational process because of the duct's symmetry, as shown in Figure 3b. Figure 3b presents schematic diagrams of the cross-sectional planes along the  $z$ -axis, at which computed data are presented.

Figure 4a shows the extended computational domain of the circular duct along the  $x$ -direction (flow), where  $h$  is the overall height (diameter) in the  $y$ -direction,  $L$  is the duct length in the  $x$ -direction, and  $b$  is the desiccant bed thickness. One-quarter of the duct structure is used in the computational process because of the duct's symmetry, as shown in Figure 4b. Figure 4b presents schematic diagrams of the cross-sectional planes along the  $z$ -axis, at which computed data are presented. The actual dimensions of all these ducts are presented in the legends of the results figures.

## 3. Governing Equations

**3.1. Assumptions.** The following assumptions are used:

- A 3-dimensional axisymmetric problem.
- Laminar flow.
- Transient velocity, temperature, and concentration fields.
- Constant properties since their variations with the temperature in our temperature range of interest are very small. For



**Figure 4.** Circular duct with (a) extended computational domain along the  $x$ -direction and (b) with two cross-sectional areas along the  $z$ -axis (one-quarter of circular duct).

example, in our study, the temperature changes by  $\sim 4$  °C, with a corresponding air specific heat change of only  $\sim 0.39\%$ .

- No-slip boundary condition for the axial velocity component  $u$  and suction condition for both  $v$  and  $w$  velocity at the desiccant surface.

- Adiabatic desiccant outer surface.

- Continuity of heat and mass flux and temperature at the fluid–solid interface.

- Negligible heat or mass flux in the desiccant bed in the  $x$ -direction. We have computed in this study that the gradient  $(\partial T/\partial x)$  is 86% and 88% smaller than  $(\partial T/\partial y)$  and  $(\partial T/\partial z)$ , respectively, and that  $(\partial C/\partial x)$  is 89% and 87% smaller than  $(\partial C/\partial y)$  and  $(\partial C/\partial z)$ , respectively.

**3.2. Fundamental Equations. 3.2.1. Region I: Air and Water Vapor.** The computational domain of the square duct in the  $x$ -direction (flow) is starting from 0 upstream and goes to  $5L$  downstream. The duct is located at  $2L \leq x \leq 3L$ ,  $0 \leq y \leq h$ , and  $0 \leq z \leq \omega$ , as shown in Figure 2b. At its entrance to the duct, the flow is impinged on the front side of the horizontal side of the desiccant bed at  $x = 2L$ ,  $0 \leq y \leq b$ , and  $0 \leq z \leq \omega$  and on the vertical one at  $x = 2L$ ,  $0 \leq y \leq h$ , and  $0 \leq z \leq b$ . Numerical experiments have shown that extension of the computational domain by a length  $2L$  both upstream and downstream of the duct along the  $x$ -direction practically eliminated compu-

tational fluid dynamics (CFD) artifacts that would have been created by the singularities posed by the duct entrance and exit (cf. ref 2). In the computations, the square duct dimensions are 0.05 m length ( $L$ ), 0.1 m height ( $h$ ), and 0.1 m width ( $\omega$ ). The three cross-sectional planes (A–A, B–B, C–C) along the  $z$ -axis are located at  $z/\omega = 0.0464$ , 0.245, and 0.5 (see Figure 2a). The seven cross-sectional planes (D–D, E–E, F–F, G–G, H–H, I–I, and J–J) along the  $x$ -axis are located at  $x/L = 2.1$ , 2.5, 2.6, 2.7, 2.8, 2.9, and 3 (see Figure 2b).

**Continuity**

$$\frac{\partial \rho_f}{\partial t} + \frac{\partial(\rho_f u_f)}{\partial x} + \frac{\partial(\rho_f v_f)}{\partial y} + \frac{\partial(\rho_f w_f)}{\partial z} = 0 \quad (1)$$

**$x$ -Momentum**

$$\frac{\partial u_f}{\partial t} + u_f \frac{\partial u_f}{\partial x} + v_f \frac{\partial u_f}{\partial y} + w_f \frac{\partial u_f}{\partial z} = -\frac{1}{\rho_f} \frac{\partial p}{\partial x} + \nu_f \left( \frac{\partial^2 u_f}{\partial x^2} + \frac{\partial^2 u_f}{\partial y^2} + \frac{\partial^2 u_f}{\partial z^2} \right) \quad (2)$$

y-Momentum

$$\frac{\partial v_f}{\partial t} + u_f \frac{\partial v_f}{\partial x} + v_f \frac{\partial v_f}{\partial y} + w_f \frac{\partial v_f}{\partial z} = -\frac{1}{\rho_f} \frac{\partial p}{\partial y} + \nu_f \left( \frac{\partial^2 v_f}{\partial x^2} + \frac{\partial^2 v_f}{\partial y^2} + \frac{\partial^2 v_f}{\partial z^2} \right) \quad (3)$$

z-Momentum

$$\frac{\partial w_f}{\partial t} + u_f \frac{\partial w_f}{\partial x} + v_f \frac{\partial w_f}{\partial y} + w_f \frac{\partial w_f}{\partial z} = -\frac{1}{\rho_f} \frac{\partial p}{\partial z} + \nu_f \left( \frac{\partial^2 w_f}{\partial x^2} + \frac{\partial^2 w_f}{\partial y^2} + \frac{\partial^2 w_f}{\partial z^2} \right) \quad (4)$$

Energy

$$\frac{\partial T_f}{\partial t} + u_f \frac{\partial T_f}{\partial x} + v_f \frac{\partial T_f}{\partial y} + w_f \frac{\partial T_f}{\partial z} = \alpha_f \left( \frac{\partial^2 T_f}{\partial x^2} + \frac{\partial^2 T_f}{\partial y^2} + \frac{\partial^2 T_f}{\partial z^2} \right) \quad (5)$$

Mass diffusion (water vapor diffusion in the airflow)

$$\frac{\partial C_f}{\partial t} + u_f \frac{\partial C_f}{\partial x} + v_f \frac{\partial C_f}{\partial y} + w_f \frac{\partial C_f}{\partial z} = D_f \left( \frac{\partial^2 C_f}{\partial x^2} + \frac{\partial^2 C_f}{\partial y^2} + \frac{\partial^2 C_f}{\partial z^2} \right) \quad (6)$$

### 3.2.2. Region II: Silica Gel Bed.

Energy

$$\frac{\partial T_s}{\partial t} = \alpha_e \left( \frac{\partial^2 T_s}{\partial x^2} + \frac{\partial^2 T_s}{\partial y^2} + \frac{\partial^2 T_s}{\partial z^2} \right) + \frac{H_1 m'''}{c_e \rho_e} \quad (7)$$

where  $H_1$  (kJ/kg) is the sorption heat,  $m'''$  (kg/m<sup>3</sup>·s) is the water adsorption rate, and  $c_w \rho_w$  is the thermal capacity of desiccant.

$$c_e \rho_e = \sigma c_f \rho_f + (1 - \sigma) c_s \rho_s \quad (8)$$

Water vapor diffusion

$$\frac{\partial C_s}{\partial t} = \frac{D_f}{\sigma} \left( \frac{\partial^2 C_s}{\partial x^2} + \frac{\partial^2 C_s}{\partial y^2} + \frac{\partial^2 C_s}{\partial z^2} \right) - \frac{m'''}{\sigma \rho_f} \quad (9)$$

The water adsorption rate in the silica gel is expressed as

$$m''' = (1 - \sigma) \rho_s \frac{\partial W}{\partial t} \quad (10)$$

The relationship between the water content in the silica gel and the water vapor concentration at the local equilibrium,  $W = f(C, T)$ , is an empirical relation, different for each desiccant. From ref 8, the relation used for silica gel is

$$\Phi = \frac{10^5 C}{0.622 + C} \quad (11)$$

where

$$(-\Phi - 9.31077 + 0.001717651T_w^2) + (478.0868 + (9.18715 \times 10^{-5})T_1^3)w - 1417.118w^2 + 2094.818w^3 = 0 \quad (12)$$

and

$$s = 4.21429 - \frac{7.5T_w}{(237.3 + T_w)} \quad (13)$$

where  $T_w$  is the silica gel temperature (°C) and  $T_1$  is the ambient air temperature (°C).

Equations 1–12 are used to solve for the unknown parameters  $u$ ,  $v$ ,  $T$ , and  $C$  in the air flow (region I) and for  $T$ ,  $C$ ,  $w$ , and  $m'''$  in the silica gel (region II).

Overall average water content in the horizontal bed

$$W_{ave} = \frac{1}{Lb\omega} \int_0^L \int_0^b \int_0^\omega W(x, y, z) dx dy dz \quad (14)$$

Overall average water adsorption rate in the horizontal bed

$$m_{ave}''' = \frac{1}{Lb\omega} \int_0^L \int_0^b \int_0^\omega m'''(x, y, z) dx dy dz \quad (15)$$

Surface average heat transfer coefficient (x–z plane)

$$h_{q,ave} = \frac{1}{L\omega} \int_0^L \int_0^\omega h_q(x, z) dx dz \quad (16)$$

Surface average mass transfer coefficient (x–z plane)

$$h_{m,ave} = \frac{1}{L\omega} \int_0^L \int_0^\omega h_m(x, z) dx dz \quad (17)$$

Surface average pressure (y–z plane)

$$P_{ave} = \frac{1}{h\omega} \int_0^h \int_0^\omega p(y, z) dy dz \quad (18)$$

### 3.3. Boundary Conditions. 3.3.1. For the Square Duct.

Insulated bottom surface at  $y = 0$

$$\frac{\partial T_s(2L \leq x \leq 3L, 0, 0 \leq z \leq 0.5\omega, t)}{\partial y} = \frac{\partial C_s(2L \leq x \leq 3L, 0, 0 \leq z \leq 0.5\omega, t)}{\partial y} = 0 \quad (19)$$

Insulated side surface at  $z = 0$

$$\frac{\partial T_s(2L \leq x \leq 3L, 0 \leq y \leq 0.5h, 0, t)}{\partial z} = \frac{\partial C_s(2L \leq x \leq 3L, 0 \leq y \leq 0.5h, 0, t)}{\partial z} = 0 \quad (20)$$

At the fluid–solid interface, heat and mass flux continuity

$$k_f \frac{\partial T_f(2L \leq x \leq 3L, b, 0 \leq z \leq 0.5\omega, t)}{\partial y} = k_e \frac{\partial T_s(2L \leq x \leq 3L, b, 0 \leq z \leq 0.5\omega, t)}{\partial y} \quad (21)$$

$$k_f \frac{\partial T_f(2L \leq x \leq 3L, 0 \leq y \leq 0.5h, b, t)}{\partial z} = k_e \frac{\partial T_s(2L \leq x \leq 3L, 0 \leq y \leq 0.5h, b, t)}{\partial z} \quad (22)$$

$$D_f \frac{\partial C_f(2L \leq x \leq 3L, b, 0 \leq z \leq 0.5\omega, t)}{\partial y} = D_e \frac{\partial C_s(2L \leq x \leq 3L, b, 0 \leq z \leq 0.5\omega, t)}{\partial y} \quad (23)$$

$$D_f \frac{\partial C_f(2L \leq x \leq 3L, 0 \leq y \leq 0.5h, b, t)}{\partial z} = D_e \frac{\partial C_s(2L \leq x \leq 3L, 0 \leq y \leq 0.5h, b, t)}{\partial z} \quad (24)$$

No heat or mass flux in silica gel bed in the  $x$ -direction at  $x = 2L$

$$\frac{\partial T_s(2L, 0 \leq y \leq b, 0 \leq z \leq 0.5\omega, t)}{\partial x} = \frac{\partial C_s(2L, 0 \leq y \leq b, 0 \leq z \leq 0.5\omega, t)}{\partial x} = 0 \quad (25)$$

$$\frac{\partial T_s(2L, 0 \leq y \leq 0.5h, 0 \leq z \leq b, t)}{\partial x} = \frac{\partial C_s(2L, 0 \leq y \leq 0.5h, 0 \leq z \leq b, t)}{\partial x} = 0 \quad (26)$$

No heat or mass flux in  $x$ -direction at  $x = 3L$

$$\frac{\partial T_s(3L, 0 \leq y \leq b, 0 \leq z \leq 0.5\omega, t)}{\partial x} = \frac{\partial C_s(3L, 0 \leq y \leq b, 0 \leq z \leq 0.5\omega, t)}{\partial x} = 0 \quad (27)$$

$$\frac{\partial T_s(3L, 0 \leq y \leq 0.5h, 0 \leq z \leq b, t)}{\partial x} = \frac{\partial C_s(3L, 0 \leq y \leq 0.5h, 0 \leq z \leq b, t)}{\partial x} = 0 \quad (28)$$

No-slip

$$u_f(2L \leq x \leq 3L, 0 \leq y \leq b, 0 \leq z \leq 0.5\omega, t) = 0 \quad (29)$$

$$u_f(2L \leq x \leq 3L, 0 \leq y \leq 0.5h, 0 \leq z \leq b, t) = 0 \quad (30)$$

Bed suction (flow transport through the bed)

$$v_s(2L \leq x \leq 3L, 0 \leq y \leq b, 0 \leq z \leq 0.5\omega, t) = \frac{m'''(2L \leq x \leq 3L, 0 \leq y \leq b, 0 \leq z \leq 0.5\omega, t)}{\rho_f} \Delta y \quad (31)$$

$$w_s(2L \leq x \leq 3L, 0 \leq y \leq 0.5h, 0 \leq z \leq b, t) = \frac{m'''(2L \leq x \leq 3L, 0 \leq y \leq 0.5h, 0 \leq z \leq b, t)}{\rho_f} \Delta z \quad (32)$$

Upstream condition

$$u_f(0, y, z, t) = u_\infty \quad (33)$$

$$v_f(0, y, z, t) = w_f(0, y, z, t) = 0 \quad (34)$$

$$T(0, y, z, t) = T_\infty \quad (35)$$

$$C(0, y, z, t) = C_\infty \quad (36)$$

Downstream condition

$$\frac{\partial u_f(5L, y, z, t)}{\partial x} = \frac{\partial v_f(5L, y, z, t)}{\partial x} = \frac{\partial w_f(5L, y, z, t)}{\partial x} = 0 \quad (37)$$

$$\frac{\partial T_f(5L, y, z, t)}{\partial x} = \frac{\partial C_f(5L, y, z, t)}{\partial x} = 0 \quad (38)$$

Top (midduct, i.e., symmetry line at  $y = 0.5h$ ) condition for the duct, which is the symmetry condition

$$\frac{\partial u_f(x, y = 0.5h, z, t)}{\partial y} = \frac{\partial T_f(x, y = 0.5h, z, t)}{\partial y} = \frac{\partial C_f(x, y = 0.5h, z, t)}{\partial y} = 0 \quad (39)$$

$$v_f(x, y = 0.5h, z, t) = w_f(x, y = 0.5h, z, t) = 0 \quad (40)$$

Side (midduct, i.e., symmetry line at  $z = 0.5\omega$ ) condition for the duct, which is the symmetry condition

$$\frac{\partial u_f(x, y, z = 0.5\omega, t)}{\partial z} = \frac{\partial T_f(x, y, z = 0.5\omega, t)}{\partial z} = \frac{\partial C_f(x, y, z = 0.5\omega, t)}{\partial z} = 0 \quad (41)$$

$$v_f(x, y, z = 0.5\omega, t) = w_f(x, y, z = 0.5\omega, t) = 0 \quad (42)$$

### 3.4. Initial Condition.

$$u_f(x, y, z, 0) = u_\infty \quad (43)$$

$$T_f(x, y, z, 0) = T_\infty \quad (44)$$

$$C_f(x, y, z, 0) = C_\infty \quad (45)$$

$$C_s(2L \leq x \leq 3L, y \leq b, 0 \leq z \leq 0.5\omega, 0) = C_b \quad (46)$$

$$W(2L \leq x \leq 3L, y \leq b, 0 \leq z \leq 0.5\omega, 0) = f(C_b, T_\infty) \quad (47)$$

The boundary and initial conditions for both the triangular and circular ducts are the same as the conditions for the square duct except that the circular duct conditions are in cylindrical coordinates.

### 4. Method of Solution And Its Validation

The continuity and momentum equations were solved by the SIMPLER (semi-implicit method for pressure-linked equation revised) algorithm control-volume method.<sup>9</sup> The numerical method was validated here by checking the grid-dependence and the convergence (in ref 10). Both the average and maximal relative errors in the computed  $u$  velocity as a function of grid size were computed as a function of the grid size and plotted.<sup>10</sup> The average relative error is defined as

$$E_{r,ave,big} = \frac{1}{i \times j} \sum_{i,j} \frac{u_{big(i,j)} - u_{small(i,j)}}{u_{big(i,j)}} \quad (48)$$

where  $u_{big(i,j)}$  and  $u_{small(i,j)}$  are the  $u$  velocities of the big and small grid sizes in the  $x$ - and  $y$ -directions, respectively, and  $i$  and  $j$  are the grid points numbers in the  $x$ - and  $y$ -directions. The maximum relative error ( $E_{r,max}$ ) is the maximum among the relative errors in the computational domain. Both errors are seen to decrease as the grid size (spacing) decreases in an asymptotic way, proving grid-independence at a grid of 250 points in the  $x$ -direction and of 150 points in the  $y$ -direction. The computational error at that grid, which was used in the computations in this paper, was  $1 \times 10^{-4}$ . The convergence of  $E_r$  was also analyzed and proven. About 46 iterations are needed

**Table 1. Comparisons of  $(fRe)$  and  $Nu_H$  of Fully Developed Laminar Flow for Square and Circular Ducts from the Present Study and Experimental Results Found in the Literature**

shape	$(fRe)$			$Nu_H$		
	present study	ref 11	error (%)	present study	ref 11	error (%)
square	14.56	14.227	2.34	3.53	3.608	2.2
circular	16.33	16	2.06	4.25	4.364	2.68

for convergence, and the number of iterations used is 120–250, depending on the case being solved.

Experimental validation of the results is difficult because there are no experimental data for such flows in such channels. Yet, besides the above-described validation of the numerical approach, this model was, therefore, validated in two additional ways: We found in ref 11 experimental data for the values of  $(fRe)$  and  $Nu_H$  in fully developed flow with heat transfer in square and circular ducts without desiccant, where  $f$  is the skin friction coefficient and  $Nu_H$  is the Nusselt number for uniform heat flux, defined as

$$f = \frac{(dp/dx)D_h}{4(1/2)\rho_f u_{f,ave}^2} = \frac{D_h \Delta p}{2\rho_f u_{f,ave}^2 L} \quad (49)$$

$$Nu_H = \frac{h_q D_h}{k_f} \quad (50)$$

where  $D_h$  is the hydraulic diameter,  $k_f$  is the fluid thermal conductivity, and  $u_{f,ave}$  is the flow  $x$ -component velocity defined as

$$u_{f,ave} = \frac{1}{A} \int_A u_f dA \quad (51)$$

where  $A$  is the  $y$ – $z$  plane cross-sectional area for the duct. We note that  $(fRe)$  is a constant for hydrodynamically fully developed laminar flow in ducts and the local Nusselt number in the thermal entry region decays along the channel and approaches a constant value asymptotically. Using our model, we computed these values for the same conditions by considering the flow to be fully developed and the internal wall of the ducts to be coated with the desiccant. The computation here is performed for the square and circular ducts. The comparisons are presented in Table 1. The agreement was found to be within 2.7%.

The second way in which we validated this model was by comparison with the results from our two-dimensional model<sup>2</sup> of the conjugate-transient two-dimensional heat and mass transfer problem between a flat-plate silica gel bed and transient humid laminar air stream, which was, by itself, successfully validated by comparison with the theoretical and experimental models of Pesaran and Mills,<sup>12,13(run1)</sup> for the system and conditions they used. This method of validation is relevant since the three-dimensional model in our paper is very similar to our two-dimensional one, having the same model configuration, method of solution, and governing equations. The comparison of the predictions by our conjugate and nonconjugate models of the outlet temperature and concentration as a function of time demonstrates close agreement with theirs, within 1.5 °C for the temperature and 8% for the concentration.<sup>2</sup>

## 5. Results and Discussions

**5.1. Flow Field Results for a Square Duct.** The flow field in the duct determines the convective mass and heat transport

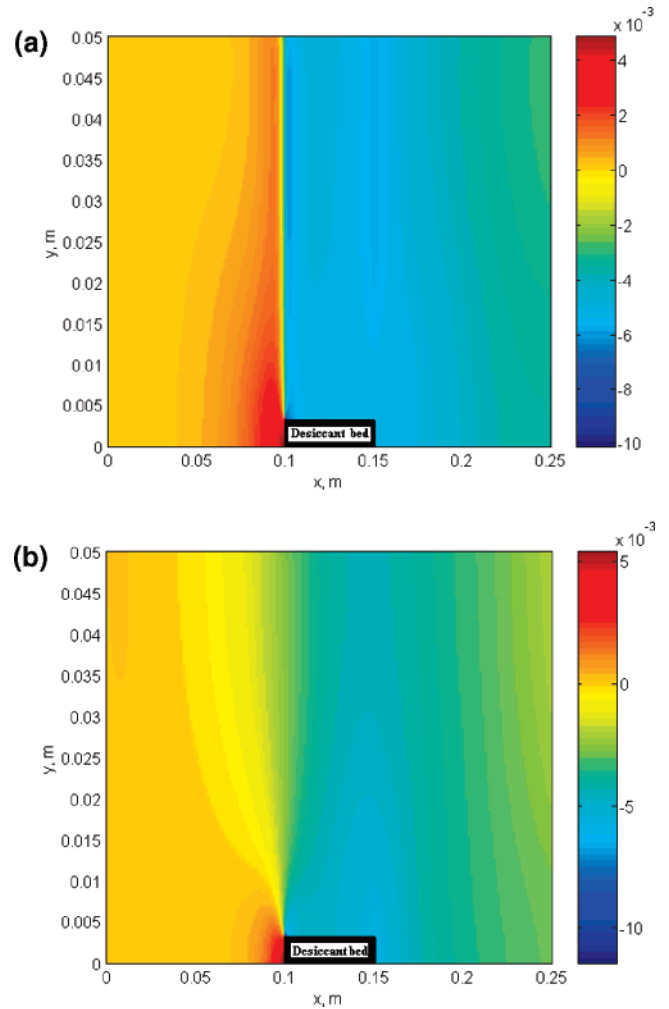


**Figure 5.** Relative pressure  $p_r$  (Pa) in the total computational domain for a square duct geometry at three different cross sections along  $z$ -axis,  $u_\infty = 0.1$  m/s,  $Re = 666$ ,  $T_\infty = 30$  °C,  $C_\infty = 0.0276$  kg/kg,  $C_b = 0.0075$  kg/kg,  $W_o = 0.1$  kg/kg,  $t = 3$  s,  $b = 0.00321$  m,  $L = 0.05$  m,  $h_\square = 0.1$  m,  $\omega = 0.1$  m,  $P_{ref} = 1.43 \times 10^{-4}$  Pa,  $\Delta p_{ave} = 1.08 \times 10^{-3}$  Pa: (a) A–A cross section at  $(x, y, z/\omega = 0.0464)$  and (b) C–C cross section at  $(x, y, z/\omega = 0.5)$ .

rates at the flow–desiccant interface and is, thus, important to understand. This is especially important for the square and triangular duct geometries, where the flows in the corner regions are more complex. Accordingly, we show pressure and velocity fields. All the flow field figures represent the simultaneous effects of dehumidification (heat and mass transfer at the wall). We note that the dehumidification process has a negligible effect on the primary flow fields, but it of course adds a velocity component perpendicular to the desiccant surface, which is zero when no dehumidification takes place.

Figure 5 shows the relative pressure,  $p_r$ , distribution

$$p_r(x,y,z) = p_g(x,y,z) - p_{g,ref}(x_o, y_o, z_o) \quad (52)$$

where the gauge reference pressure,  $p_{g,ref}$  ( $=1.43 \times 10^{-4}$  Pa), is chosen to be that at the coordinates origin in the total computational domain (using extended domain computation) at different  $x$ – $y$  planes (A–A and C–C) along the  $z$ -axis (see Figures 1 and 2). We made the ordinate in Figure 5 almost 3 times larger than the abscissa to present more detail about the flow behavior in the  $y$ -direction. The relative pressure inside the square duct at different  $y$ – $z$  planes (D–D, I–I, and J–J) along the  $x$ -axis is shown in Figure 6.

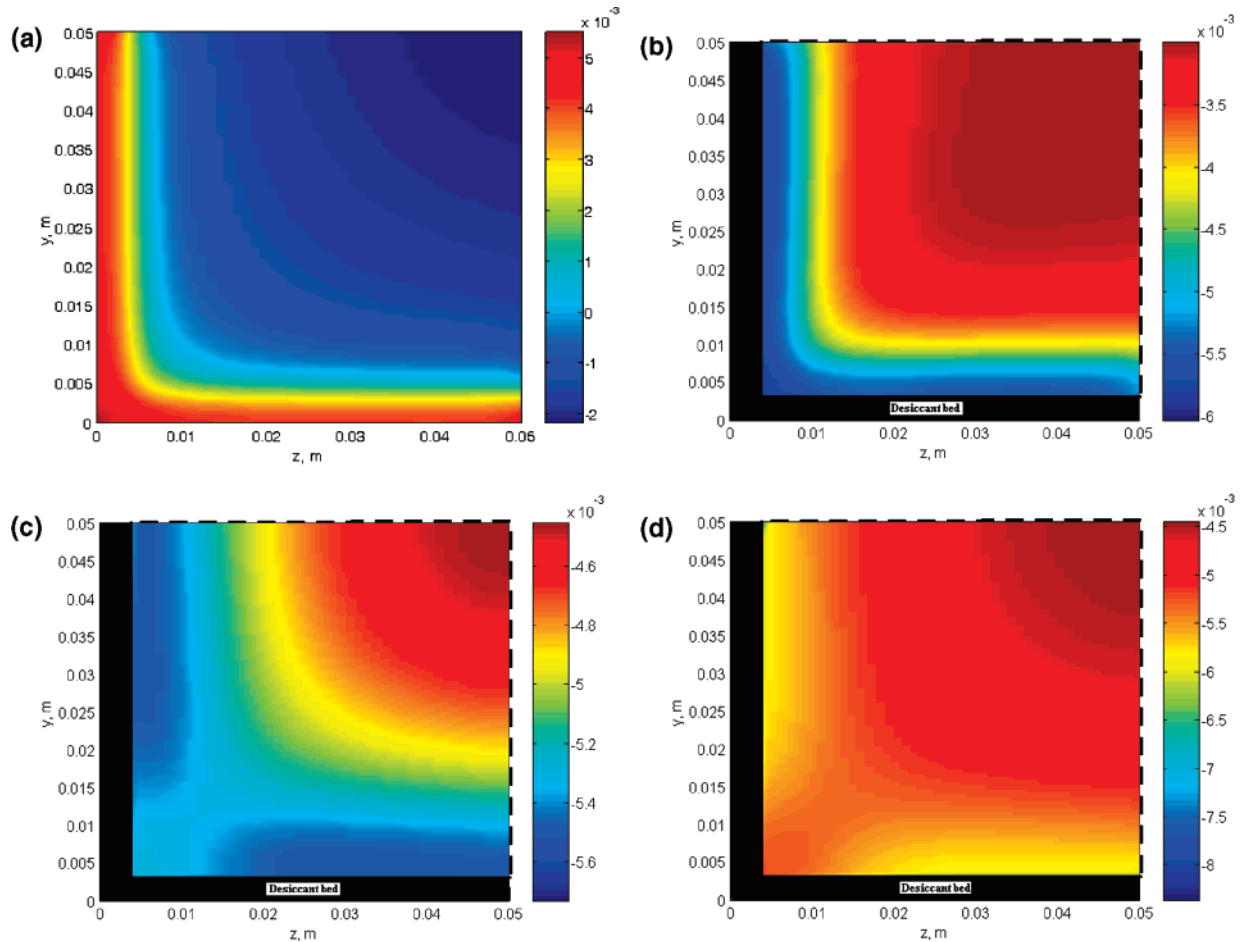


**Figure 6.** Relative pressure  $p_r$  (Pa) inside a square duct at different cross sections along  $x$ -axis,  $u_\infty = 0.1$  m/s,  $Re = 666$ ,  $T_\infty = 30$  °C,  $C_\infty = 0.0276$  kg/kg,  $C_b = 0.0075$  kg/kg,  $W_o = 0.1$  kg/kg,  $t = 3$  s,  $b = 0.00321$  m,  $L = 0.05$  m,  $h_\square = 0.1$  m,  $\omega = 0.1$  m,  $P_{ref} = 1.43 \times 10^{-4}$  Pa,  $\Delta p_{ave} = 1.08 \times 10^{-3}$  Pa: (a)  $y$ - $z$  plane in front of the duct entrance at  $(x/L = 1.9, y, z)$ ; (b) D-D cross section at  $(x/L = 2.1, y, z)$ ; (c) I-I cross section at  $(x/L = 2.9, y, z)$ ; and (d) J-J cross section at  $(x/L = 3, y, z)$ .

Figure 5 shows that the relative pressure rises upstream of the duct leading edge, because of stagnation of the stream as it impinges on the duct. At the upstream of the duct leading edge ( $x = 0.09$  m and  $y = 0.001$  m) for the two  $x$ - $y$  planes (A-A and C-C) along the  $z$ -axis, the relative pressure drops with  $z$ , by 23% from  $z = 0.00464$  to  $0.05$  m. The relative pressure upstream of the duct leading edge ( $x = 0.09$  and  $y = 0.01$  m,  $z = 0.05$  m) in the C-C cross section (Figure 5b) is about twice as large as that inside the duct and the downstream region. The relative pressure recovers and builds up downstream inside the duct, and it rises as  $y$  and  $z$  increases toward the duct centerline, where the maximum axial flow velocity exists. Further detail about the change in relative pressure in both the  $y$ - and  $z$ -directions is presented in Figure 6. For example, the relative pressure in the I-I cross section along the  $x$ -axis as shown in Figure 6c (at  $x/L = 2.9$  and  $y = 0.015$  m) increases about 8% as  $z$  increases from  $0.00464$  to  $0.05$  m. Parts b and c of Figure 6 show that the relative pressure inside the duct drops by about 30–35% along the  $x$ -axis from  $0.105$  m ( $x/L = 2.1$ ) to  $0.145$  m ( $x/L = 2.9$ ), because of flow friction. However, the relative pressure increases at  $x = 0.15$  m ( $x/L = 3$ , trailing edge) because of the increase in the  $(\partial u/\partial y)$  and  $(\partial u/\partial z)$  at the surface, which results in a high shear stress, as shown in Figure 6d.

Figures 7 and 8 show the total flow velocity vectors and magnitudes (eq 53) in the whole computational domain ( $0 \leq x \leq 5L$ ,  $L = 0.05$  m) for the square duct geometry (see Figure 1) and over the horizontal bed of the duct ( $2L \leq x \leq 3L$ ,  $L = 0.05$  m) at two different  $x$ - $y$  cross sections (A-A and C-C as shown

in Figure 2a) along the  $z$ -axis, respectively. The total flow velocity magnitude in the  $x$ - and  $y$ -directions is defined as

$$V = \sqrt{u^2 + v^2 + w^2} \quad (53)$$

The total velocity has nearly the same direction and magnitude of the axial ( $u$ ) velocity since  $v$  and  $w$  are small compared with  $u$ : over the bed and in the boundary layer region, from near the bed surface to the outside of the boundary layer,  $v/u = 0.0606$ – $0.0323$  at the leading-edge region and  $0.0263$ – $0.0158$  at the trailing edge.  $V$  also increases along the  $z$ -axis from the wall toward the center ( $z = 0.00464$ – $0.05$  m) because of the retarding effect of the walls.

Figure 8 shows the flow region presented in Figure 7, enlarged to provide more detail in the desiccant region. The magnitude of  $V$  is 90–100% of the free air stream velocity ( $u_\infty = 0.1$  m/s) at the duct entrance, where the velocity gradient in the  $y$ -direction is large, as shown in Figure 8a. It drops at  $x = 0.105$  m to reach 20–40%, since this cross section (A-A) is located adjacent to the vertical desiccant bed surface of the square duct, where the boundary layer region of that vertical bed exists. The high velocity gradient at the surface of that vertical bed results in a high shear stress, and it drops with increasing  $x$ . Figure 8b shows the development of the boundary layer over the horizontal desiccant bed of the square duct at the C-C cross sections located far from the vertical desiccant bed.

Parts a–d of Figure 9 show the  $V$  magnitudes (eq 53) based on the color scale and the vectors of the velocities in the cross

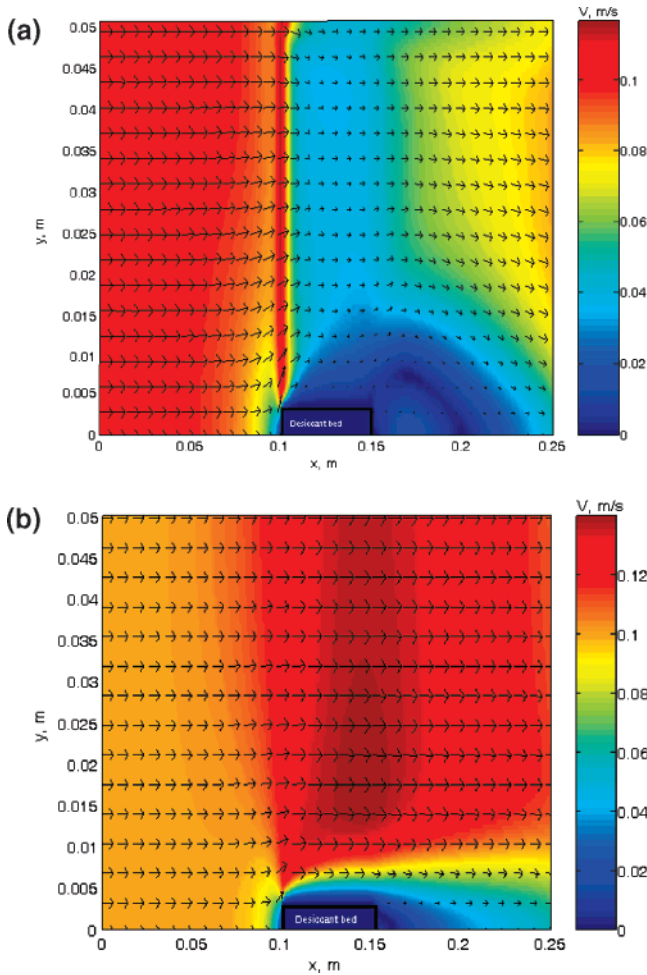


**Figure 7.** Total flow velocity distribution  $V$  in the total computational domain ( $0 \leq x \leq 5L$ ) for a square duct geometry at two different cross sections,  $u_\infty = 0.1$  m/s,  $Re = 666$ ,  $T_\infty = 0$  °C,  $C_\infty = 0.0276$  kg/kg,  $C_w = 0.0075$  kg/kg,  $W_0 = 0.1$  kg/kg,  $t = 3$  s,  $b = 0.00321$  m,  $L = 0.05$  m,  $h_\square = 0.1$  m,  $\omega = 0.1$  m,  $P_{ref} = 1.43 \times 10^{-4}$  Pa,  $\Delta p_{ave} = 1.08 \times 10^{-3}$  Pa: (a) A–A cross section at  $(x, y, z/\omega = 0.0464)$  and (b) C–C cross section at  $(x, y, z/\omega = 0.5)$ .

section  $y$ – $z$  (composites of the  $v$  and  $w$  velocities) inside the square duct along the  $x$ -axis (see Figure 2b). Noting that the flow enters the duct from a much broader cross section and then exits the channel to a much broader cross section, one can observe the following main phenomena.

(1) The flow constriction and slowdown due to the duct walls causes cross-sectional velocity components from the walls toward the center, especially pronounced in the corners where the slowdown is most prominent.

(2) The axial velocity in the duct center is not the maximal in the duct, as the duct is short and the flow does not develop by the time it exits.

(3) Recirculations, affected by flow development and the duct exit where the flow diverges into the free stream, take place from the center to the walls after about  $x = 0.135$  m (Figure 9b), and they grow in magnitude with  $x$ .

In parts a–d of Figure 9, it is seen that the total velocity  $V$  has nearly the magnitude of the axial ( $u$ ) velocity since  $v$  and  $w$  are small compared with  $u$  as presented above. These figures depict that the viscous boundary layer grows downstream, retarding the axial ( $u$ ) velocity at the wall and thereby accelerating the center-core flow to maintain the incompressible continuity requirement. The total velocity  $V$  is supposed to be the higher velocity in the core region, but it was not. Fang et al.<sup>14</sup> found

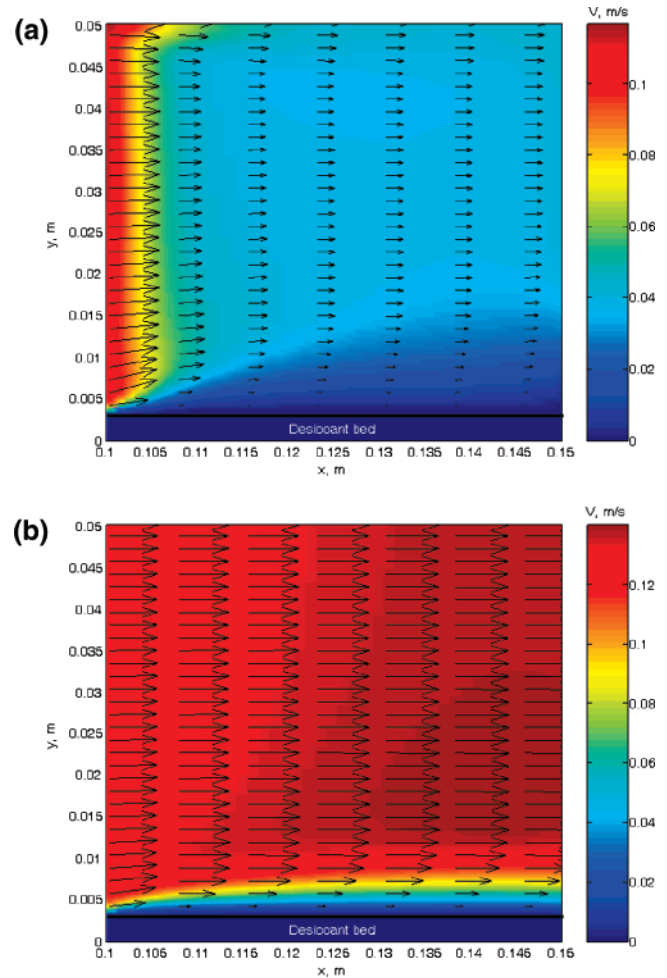


**Figure 8.** Total flow velocity distribution  $V$  over the desiccant bed ( $2L \leq x \leq 3L$ ) for a square duct geometry at two different cross sections,  $u_\infty = 0.1$  m/s,  $Re = 666$ ,  $T_\infty = 30$  °C,  $C_\infty = 0.0276$  kg/kg,  $C_w = 0.0075$  kg/kg,  $W_0 = 0.1$  kg/kg,  $t = 3$  s,  $b = 0.00321$  m,  $L = 0.05$  m,  $h_\square = 0.1$  m,  $\omega = 0.1$  m,  $P_{ref} = 1.43 \times 10^{-4}$  Pa,  $\Delta p_{ave} = 1.08 \times 10^{-3}$  Pa: (a) A–A cross section at  $(x, y, z/\omega = 0.0464)$  and (b) C–C cross section at  $(x, y, z/\omega = 0.5)$ .

experimentally at the exit of square-to-square contraction that the velocity in the core region was not the highest one. The flow here is driven by the pressure drop and the wall friction varies greatly, being largest near the midpoints of the sides and zero in the corner.

Although the  $v$  and  $w$  velocities are small, the vectors of these velocities imply continuous movement from the corners and walls to the center, as shown in parts a and b of Figure 9, and then they reverse toward the walls when approaching the trailing edge, as shown in parts c and d of Figure 9. This happens because of the boundary layer behavior and the effect of the trailing edge.

The area adjacent to the horizontal bed surface and after the corner region has approximately the same direction and magnitude of  $v$  velocity in the positive  $y$ -direction since the magnitude of  $w$  velocity is small compared to the magnitude of  $v$  velocity. This behavior indicates that the  $v$  velocity gradient in the  $y$ -direction ( $\partial v/\partial y$ ) drops along the  $y$ -axis. The total velocity in the area adjacent to the vertical bed surface and above the corner region has approximately the same direction and magnitude of  $w$  velocity in the positive  $z$ -direction since the magnitude of  $v$  velocity is small compared to the magnitude of  $w$  velocity, which indicates that the  $w$  velocity gradient in the  $z$ -direction ( $\partial w/\partial z$ ) drops along the  $z$ -axis. These two velocity gradients decrease along the  $x$ -axis because of the drop in the

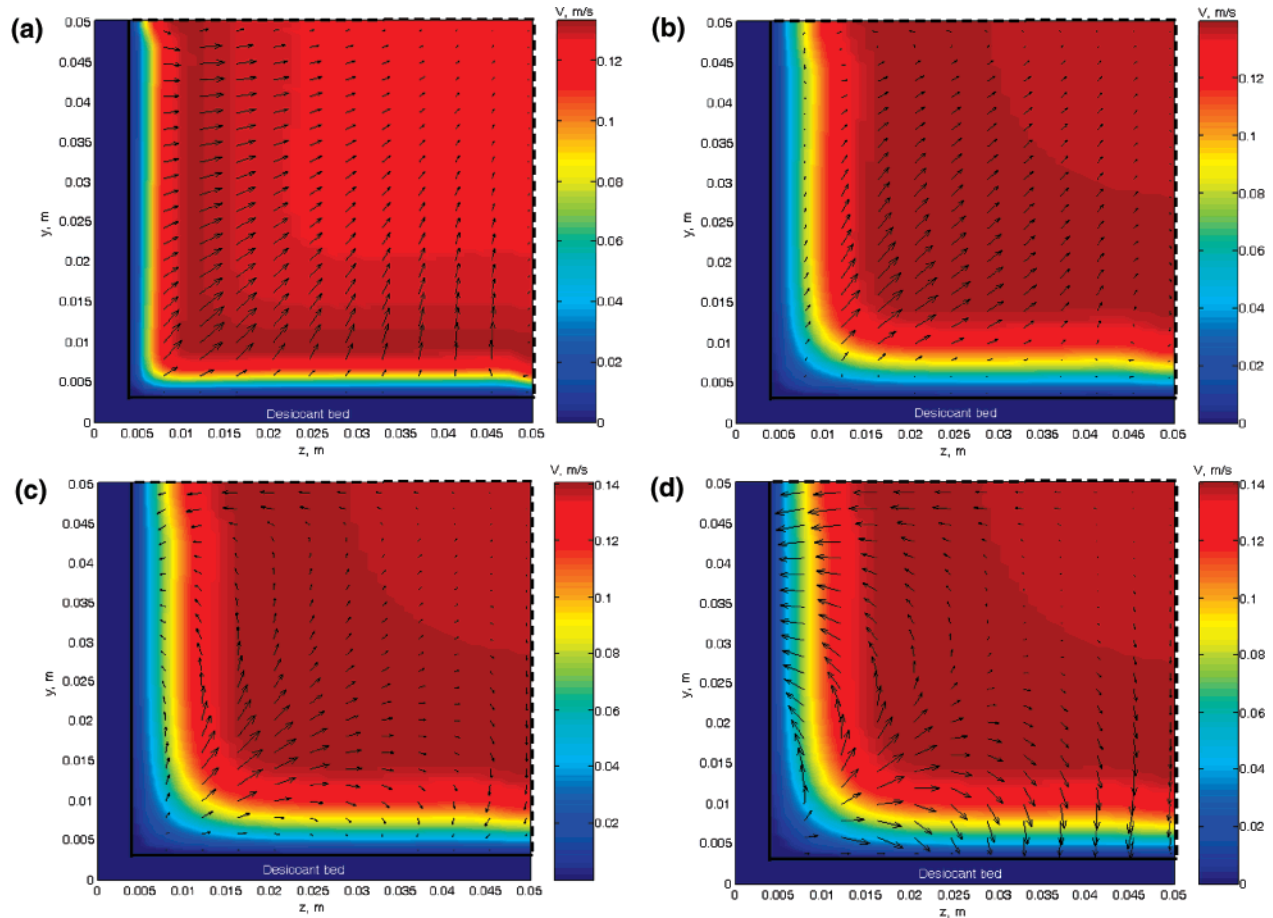


**Figure 9.** 3-D velocity field inside a square duct at different cross sections along the flow direction  $x$ . Note: the colors describe the total velocity  $V$ , and the arrows describe the velocity vectors in the  $y$ - $z$  plane,  $u_\infty = 0.1$  m/s,  $Re = 666$ ,  $T_\infty = 30$  °C,  $C_\infty = 0.0276$  kg/kg,  $C_b = 0.0075$  kg/kg,  $W_o = 0.1$  kg/kg,  $t = 3$  s,  $b = 0.00321$  m,  $L = 0.05$  m,  $h_{\square} = 0.1$  m,  $\omega = 0.1$  m,  $P_{ref} = 1.43 \times 10^{-4}$  Pa,  $\Delta p_{ave} = 1.08 \times 10^{-3}$  Pa: (a) D-D cross section at  $(x/L = 2.1, y, z)$ ; (b) G-G cross section at  $(x/L = 2.7, y, z)$ ; (c) I-I cross section at  $(x/L = 2.9, y, z)$ ; and (d) J-J cross section at  $(x/L = 3, y, z)$ .

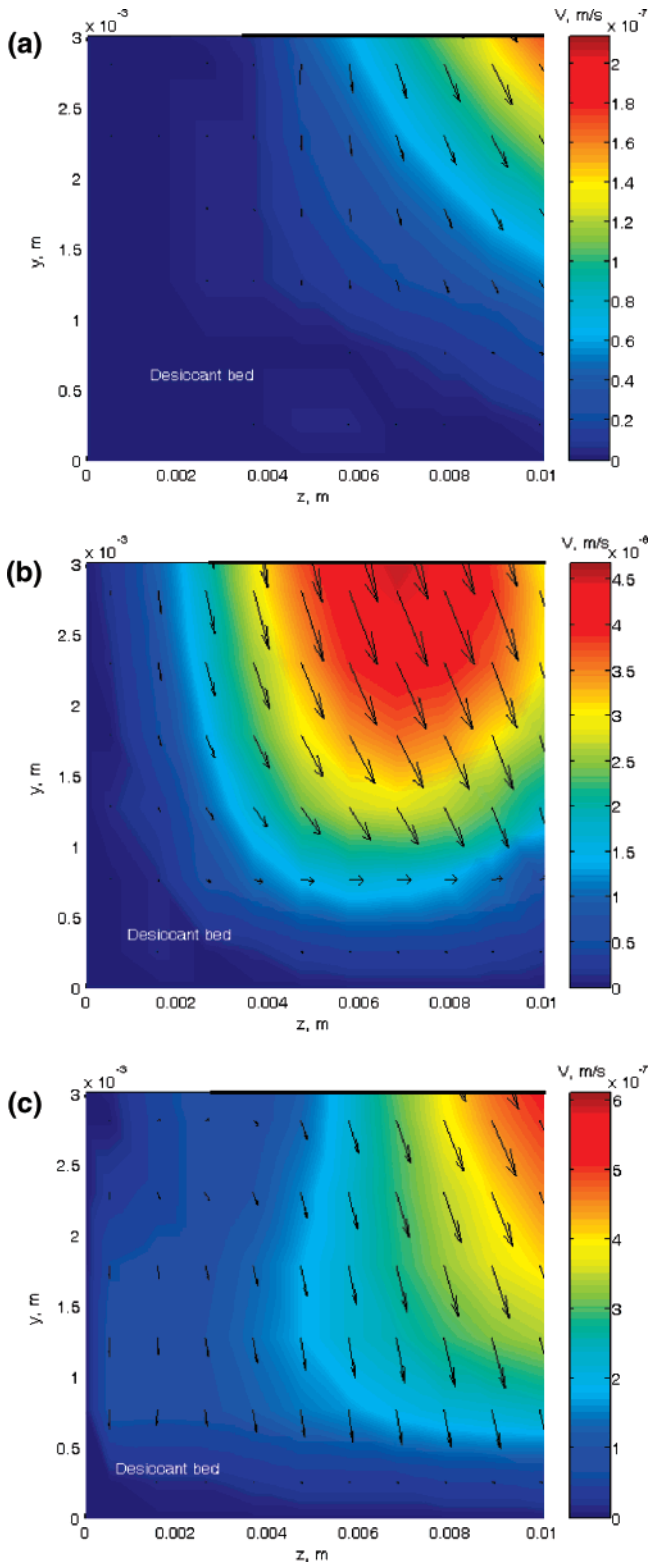
pressure (Figure 6 parts a–d). However, in the corner region, the total velocity has an almost  $45^\circ$  direction and a large magnitude, which indicates that a high velocity gradient exists because of a high shear stress. This velocity gradient decreases along the  $x$ -axis because of the drop in the pressure (Figure 6 parts a–d). The magnitude of the total velocity decreases as the flow moves along the two beds in the  $x$ -direction because of the drop in the pressure (Figure 6 parts a–d). At  $x = 0.145$  m (Figure 10c), and the direction of the flow starts changing partially toward the two beds and as it approaches the trailing edge at  $x = 0.15$  m. The total backflow becomes obvious following the downstream edge, as shown in Figure 9d, because of the increase in the pressure (see Figure 6d), which is caused by the increase in the  $u$  velocity gradient in the  $y$ - and the  $z$ -directions at the surface, resulting in a high shear stress as shown in Figure 6d. The increase in the pressure at  $x = 0.15$  m causes the pressure gradient to be high, which is needed to produce a high acceleration at the trailing edge to drive the flow downstream.

Parts a and c of Figure 10 show the total  $V$  suction velocity vectors and magnitudes (eq 53; composites of the  $v_w$ ,  $w_w$ , and  $u$  velocities) inside the horizontal desiccant bed at three different  $y$ - $z$  cross sections (D–D, E–E, and J–J) along the  $x$ -axis. The axial ( $u$ ) velocity here is equal to zero because of the no-slip boundary condition, and the other two velocities ( $v_w$  and  $w_w$ ) are much smaller than  $v$  and  $w$  velocities in the flow region. For that reason, the flow is not visible toward the bed in Figure 9. This  $V$  is presented below the corner region and at a short  $z$  distance since this region exhibits a high humid air velocity gradient, which causes the increase in the mass transport

coefficient.  $V$  inside the bed is controlled by the behavior of the water adsorption rate,  $m'''$ , since the  $v_w$  and  $w_w$  velocities are functions of  $m'''$  (eqs 31 and 32). The water adsorption rate is obviously highest adjacent to the air–desiccant interface, and it drops toward the bottom of the bed in the  $y$ -direction because of the reduction in water vapor concentration gradient in the  $y$ -direction (more details about  $m'''$  behavior in the desiccant bed is presented in Section 5.3). Therefore,  $V$  drops toward the bottom in the  $y$ -direction.  $V$  in the desiccant near the air interface increases with  $x$ , by 130% from  $x = 0.105$  to  $0.125$  m, and then it drops by 70% as  $x$  changes from  $0.125$  to  $0.15$  m because of the change in the water adsorption rate. The change in the water adsorption rate ( $m'''$ ) with  $x$  occurs because of both the water vapor transport at the desiccant bed surface and the concentration distribution in the solid desiccant. This change in  $m'''$  causes the change in the water content, with the same behavior at the bed surface. Referring to our paper,<sup>2</sup> the surface water content at the bed leading edge ( $x = 0.1$  m) is relatively large because  $(\partial u/\partial y)$  near the air–desiccant interface is large. The surface water content decays with  $x$  because of the corresponding reduction in  $(\partial u/\partial y)$ , which causes the reduction in mass transport coefficient. Since  $V$  in the bed behaves the same as  $m'''$ , then its direction takes the direction of the water penetration to a lower depth in the  $y$ -direction.

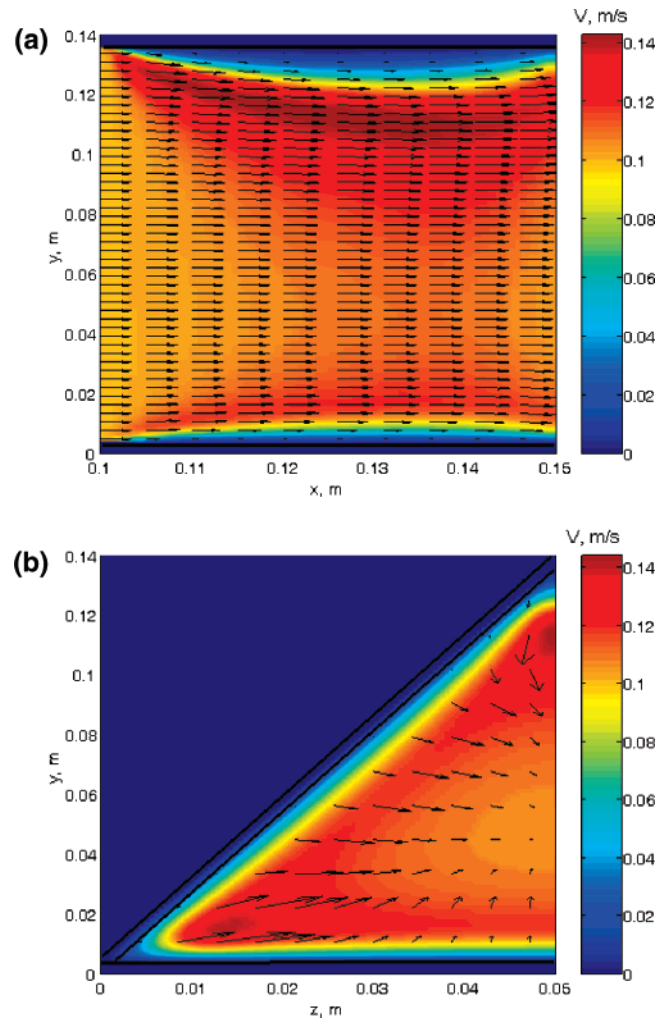
## 5.2. Flow Field Results for Triangular and Circular Ducts.

Figure 11a shows the  $V$  vectors and magnitude (eq 53) over the horizontal triangular duct at  $x$ - $y$  cross section (A–A) along the  $z$ -axis (see Figure 3b). It depicts the development of the boundary layers over both the lower (base) and the upper (side)



**Figure 10.** Total flow velocity  $V$  inside a desiccant bed at different cross sections,  $u_\infty = 0.1$  m/s,  $Re = 666$ ,  $T_\infty = 30$  °C,  $C_\infty = 0.0276$  kg/kg,  $C_b = 0.0075$  kg/kg,  $W_o = 0.1$  kg/kg,  $t = 3$  s,  $b = 0.00321$  m,  $L = 0.05$  m,  $h_\Delta = 0.1$  m,  $\omega = 0.1$  m,  $P_{ref} = 1.43 \times 10^{-4}$  Pa,  $\Delta p_{ave} = 1.08 \times 10^{-3}$  Pa: (a) D–D cross section at ( $x/L = 2.1$ ,  $0 \leq y \leq 0.003$ ,  $0 \leq z \leq 0.01$ ); (b) E–E cross section at ( $x/L = 2.5$ ,  $0 \leq y \leq 0.003$ ,  $0 \leq z \leq 0.01$ ); and (c) J–J cross section at ( $x/L = 3$ ,  $0 \leq y \leq 0.003$ ,  $0 \leq z \leq 0.01$ ).

desiccant beds of the triangular duct at the vertical symmetry cross section A–A.  $V$  has nearly the same direction and magnitude of the axial ( $u$ ) velocity since  $v$  and  $w$  are small compared with  $u$ : over the bed and in the boundary layer region, from nearby the bed surface to the outer side of the boundary



**Figure 11.** Total flow velocity  $V$  inside a triangular duct at two cross sections,  $u_\infty = 0.1$  m/s,  $Re = 466$ ,  $T_\infty = 30$  °C,  $C_\infty = 0.0276$  kg/kg,  $C_b = 0.0075$  kg/kg,  $W_o = 0.1$  kg/kg,  $t = 3$  s,  $b = 0.00321$  m,  $L = 0.05$  m,  $h_\Delta = 0.141$  m,  $\omega = 0.1$  m,  $P_{ref} = 1.43 \times 10^{-4}$  Pa,  $\Delta p_{ave} = 5.2 \times 10^{-3}$  Pa: (a) A–A cross section at ( $x, y, z/\omega = 0.5$ ) and (b) B–B cross section at ( $x/L = 2.5, y, z$ ).

layer,  $v/u = 0.072$ – $0.044$  at the leading-edge region and  $0.027$ – $0.019$  at the trailing edge. Because of the triangular cross section,  $V$  obviously increases with  $y$ ; thus, the velocity gradients increase from the triangle sides to its apexes.

Figure 11b shows the  $V$  magnitudes (eq 53) based on the color scale and the vectors of the velocities in the  $y$ – $z$  cross section (composites of the  $v$  and  $w$  velocities) inside the triangular duct along the  $x$ -axis (see Figure 3b). In this figure, it is seen that the total velocity  $V$  has nearly the magnitude of the axial ( $u$ ) velocity since  $v$  and  $w$  are small compared with  $u$ . This figure depicts that the viscous boundary layer grows downstream, retarding the axial ( $u$ ) velocity at the wall and thereby accelerating the center-core flow to maintain the incompressible continuity requirement. The flow here is driven by the pressure drop, and the wall friction varies greatly, being largest near the midpoints of the sides and zero in the corner. Although the  $v$  and  $w$  velocities are small, the vectors of these velocities show continuous movement from the corners and walls to the center, as shown in Figure 11b.

Figure 12a shows the  $V$  vectors and magnitude (eq 53) inside the circular duct at  $x$ – $y$  cross section (A–A) along the  $z$ -axis (see Figure 4b). It depicts the development of the boundary layers over the desiccant bed.  $V$  has nearly the same direction and magnitude of the axial ( $u$ ) velocity since  $v$  and  $w$  are small

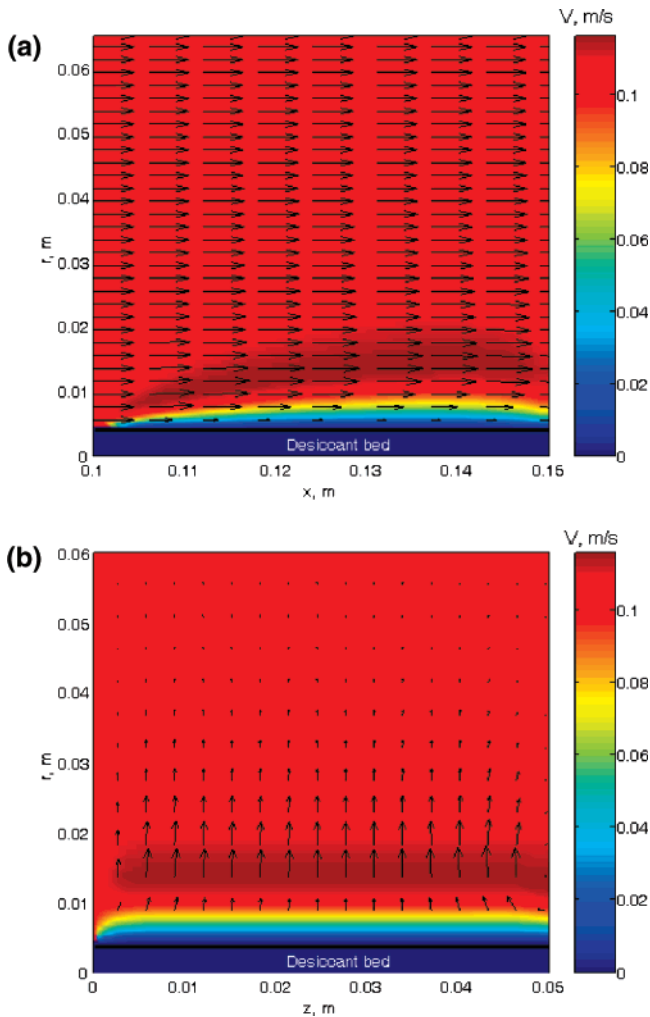


**Figure 12.** Total flow velocity  $V$  inside a circular duct at two cross sections,  $u_\infty = 0.1$  m/s,  $Re = 846$ ,  $T_\infty = 30$  °C,  $C_\infty = 0.0276$  kg/kg,  $C_b = 0.0075$  kg/kg,  $W_0 = 0.1$  kg/kg,  $t = 3$  s,  $b = 0.00321$  m,  $L = 0.05$  m,  $h_{CO} = 0.127$  m,  $\omega = 0.1$  m,  $P_{ref} = 1.43 \times 10^{-4}$  Pa,  $\Delta p_{ave} = 0.92 \times 10^{-3}$  Pa: (a) A–A cross section at  $(x, y, z/\omega = 0.5)$  and (b) B–B cross section at  $(x/L = 2.5, y, z)$ .

compared with  $u$ : over the bed and in the boundary layer region, from nearby the bed surface to the outside of the boundary layer,  $v/u = 0.066$ – $0.0381$  at the leading-edge region and  $0.0267$ – $0.017$  at the trailing edge.

Figure 12b show the  $V$  magnitudes (eq 53) based on the color scale and the vectors of the velocities in the  $y$ – $z$  cross section (composites of the  $v$  and  $w$  velocities) inside the circular duct along the  $x$ -axis (see Figure 4b). In this figure, it is seen that the total velocity  $V$  has nearly the magnitude of the axial ( $u$ ) velocity since  $v$  and  $w$  are small compared with  $u$ . This figure depicts that the viscous boundary layer grows downstream, retarding the axial ( $u$ ) velocity at the wall and thereby accelerating the center-core flow to maintain the incompressible continuity requirement. The flow here is driven by the pressure drop, and the wall friction varies greatly, being largest near the midpoints of the sides and zero in the corners.

**5.3. Heat and Mass Transfer Results.** For the adsorption process, parts a–d of Figure 13 show the time dependence of the desiccant surface water concentration and surface temperature at  $x = 0.11$  m ( $0.2L$  from the leading edge of the duct),  $y = b$ , and  $z = 0.05$  m ( $z/\omega = 0.5$ ), as well as the overall average water contents and adsorption rates for three duct geometries. As expected, all of these quantities increase more rapidly at

first and then increase at a slower rate as the bed becomes increasingly water-laden and, thus cannot take up vapor as rapidly. The time step used in these computations is 0.1 s, within which the extremely rapid adsorption by the desiccant occurs because of the sudden increase in the velocity gradient ( $\partial u/\partial y$ ) near the desiccant bed surface. This increase in the velocity gradient is caused by the flow encounter with the leading edge of the duct. The convective heat and mass transfer coefficients are related to the velocity gradient ( $\partial u/\partial y$ ) through the temperature and concentration gradients in the  $y$ -direction. Because of the local equilibrium relations, the water content exhibits a similar behavior as that of the temperature and concentration. An initial rise in the water adsorption rate occurs because of the rapid rise in the water content. The adsorption rate then decays rapidly and becomes asymptotic as the time increases because of the slow increase in the water content. The magnitudes of the surface concentration, the surface temperature, the overall average water content, and the adsorption rate for the circular duct at  $t = 3$  s are 1.05%, 0.17 °C, 5.6%, and 22% larger than those for the square duct, and 0.73%, 0.1 °C, 2.4%, and 9.8% smaller than those for the triangular duct, respectively. This is due to the duct cross section geometry related changes in the mass transport coefficient, resulting from the change in the ( $\partial u/\partial y$ ) near the desiccant bed at  $x = 0.11$  m and  $z = 0.05$  m, as presented in Table 2.

The equations used in this model are valid as long as the desiccant has not reached a state beyond saturation. Silica gel reaches saturation when the water content is 38% at 100%  $\phi$  (relative humidity), which occurs at  $T = 65.7$  °C according to the silica gel isotherm, eq 12. The analysis in our paper<sup>2</sup> for flow passing the desiccant bed shows that the average maximal water content is reached at  $t = 20$  s and  $b = 3.21$  mm and amounts to  $\sim 11.2\%$ , indicating that the silica gel did not reach saturation; thus, water condensation effects do not need to be considered in this model.

The average water content for the triangular duct at  $t = 3$  s is  $\sim 11.9\%$ , as shown in Figure 13c, which indicates that the silica gel does not reach the saturation state because it saturates when the water content is 38% at 100%  $\phi$  (relative humidity), which is obtained at  $T = 65.7$  °C according to the silica gel isotherm, eq 12.

Parts a–c of Figure 14 show the water adsorption rate  $m'''$  inside the horizontal desiccant bed at  $x$ – $y$  cross section A–A (Figure 2a) along the  $x$ -axis (Figure 14a) and at two different  $y$ – $z$  cross sections (D–D and J–J) along the  $z$ -axis (Figures 14 parts b and c). This shows that  $m'''$  is large at the duct entrance, especially near the air–desiccant interface, following the magnitude of ( $\partial u/\partial y$ ). The water adsorption rate  $m'''$  inside the desiccant is seen to decrease from the bed surface down toward its bottom, and the water penetrates gradually deeper with  $x$ , as expected. It is noteworthy that the adsorption rate is very small near the duct vertical wall.

Parts a and b of Figure 15 show that  $m'''$  and  $W$  change with  $x$  at the desiccant surface ( $y = 0.00321$  m and  $z = 0.05$  m), respectively. Both the surface  $m'''$  and  $W$  at the bed leading edge ( $x = 0.1$  m) are relatively large because ( $\partial u/\partial y$ ) near the air–desiccant interface is large. The surface  $m'''$  and  $W$  decay with  $x$  because of the corresponding reduction in transport rates, which depend on ( $\partial u/\partial y$ ). It is noteworthy here that the surface  $W$  increases slightly toward the end of the plate ( $x = 0.148$ – $0.15$  m), in the vicinity of the trailing edge ( $x = 0.15$  m), because of the increase in the local mass transport coefficient (see Figure 17b).

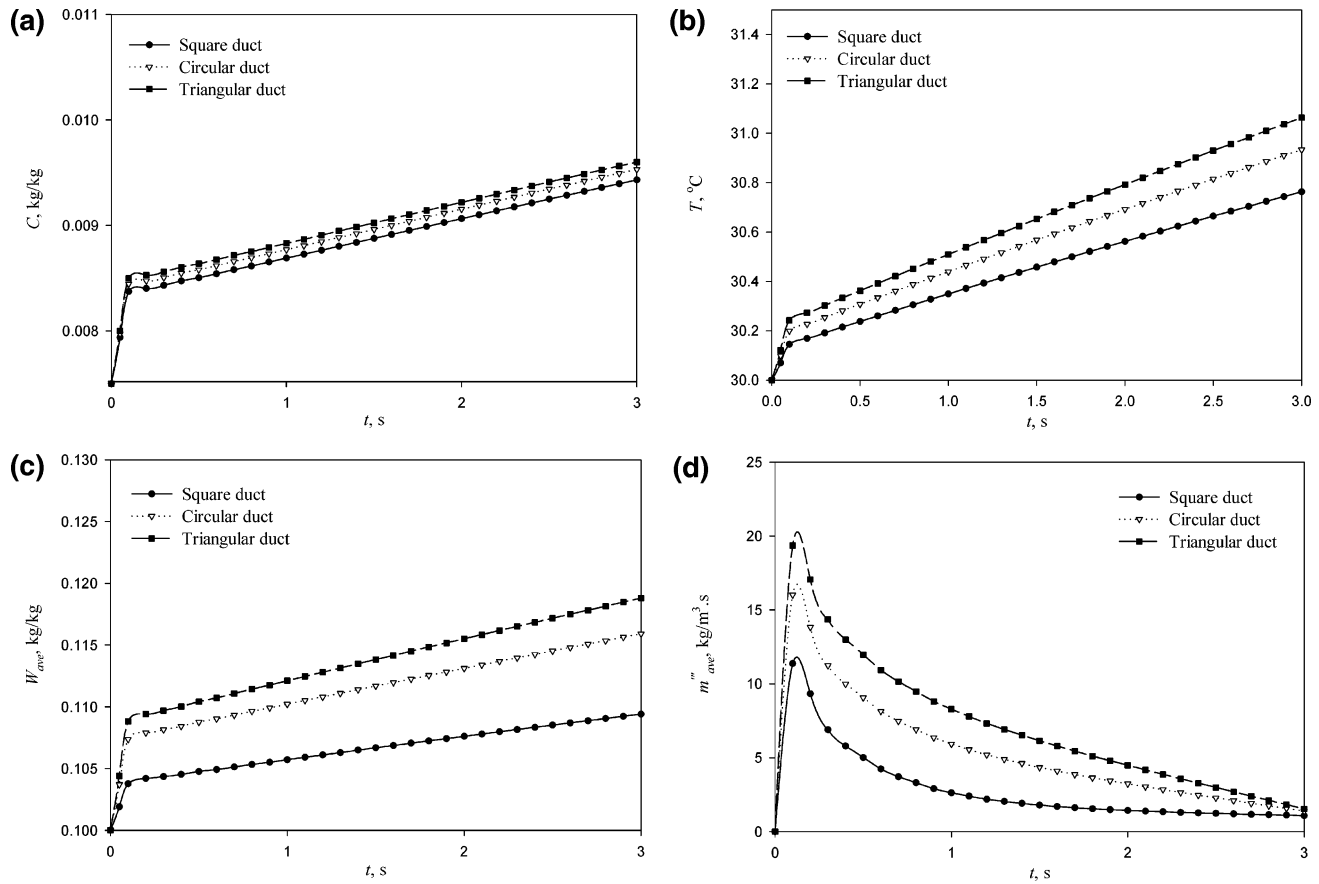


**Figure 13.** Time dependence of the desiccant surface ( $y = b$ ) (a) water concentration ( $x = 0.11$  m and  $z = 0.05$  m), (b) temperature ( $x = 0.11$  m and  $z = 0.05$  m), (c) overall average water content, and (d) overall average water adsorption rate for three duct cross-sectional shapes,  $u_\infty = 0.1$  m/s,  $Re = 666$  (square),  $Re = 466$  (triangular),  $Re = 846$  (circular),  $T_\infty = 30$  °C,  $C_\infty = 0.0276$  kg/kg,  $C_w = 0.0075$  kg/kg,  $W_o = 0.1$  kg/kg,  $t = 3$  s,  $b = 0.00321$  m,  $L = 0.05$  m,  $h_\Delta = 0.141$  m,  $h_\square = 0.127$  m,  $h_\triangle = 0.1$  m,  $\omega = 0.1$  m,  $P_{ref} = 1.43 \times 10^{-4}$  Pa.

**Table 2.** Area-Averaged Parameters That Affect the Adsorption Process for the Three Duct Geometries, Computed for the Same Inlet Air Flow Velocity and Desiccant Surface Area of All Three Ducts<sup>a</sup>

duct type	$(\partial u/\partial y)_{ave}$ , 1/s	$\Delta p_{ave}$ , Pa = $p_{ave(x=0.10,y,z)} - p_{ave(x=0.15,y,z)}$	$h_{q,ave}$ , kW/m <sup>2</sup> ·°C ( $x, y = 0.003$ m, $z$ )	$h_{m,ave}$ , kg/m <sup>2</sup> ·s ( $x, y = 0.003$ m, $z$ )
triangular	7.18	$3.47 \times 10^{-3}$	$4.63 \times 10^{-3}$	$4.8 \times 10^{-3}$
circular	6.6	$0.92 \times 10^{-3}$	$4.25 \times 10^{-3}$	$4.4 \times 10^{-3}$
square	5.77	$1.08 \times 10^{-3}$	$3.65 \times 10^{-3}$	$3.78 \times 10^{-3}$

<sup>a</sup>  $u_\infty = 0.1$  m/s,  $Re = 666$  (square),  $Re = 466$  (triangular),  $Re = 846$  (circular),  $T_\infty = 30$  °C,  $C_\infty = 0.0276$  kg/kg,  $C_w = 0.0075$  kg/kg,  $W_o = 0.1$  kg/kg,  $t = 3$  s,  $b = 0.00321$  m,  $L = 0.05$  m,  $h_\Delta = 0.141$  m,  $h_\square = 0.127$  m,  $h_\triangle = 0.1$  m,  $\omega = 0.1$  m,  $P_{ref} = 1.43 \times 10^{-4}$  Pa,  $A_s = 0.02$  m<sup>2</sup>.

Parts a and b of Figure 16 show that the  $m'''$  and  $W$  change with  $z$  at the desiccant surface ( $y = 0.00321$  m and  $x = 0.105$  m), respectively. Both  $m'''$  and  $W$  increase starting from the corner region along the horizontal desiccant bed toward the duct center at  $z = 0.05$  m because of the corresponding increase in transport rates, which depend on  $(\partial u/\partial y)$ . It is noteworthy here that both  $m'''$  and  $W$  drop slightly toward the center because of the flow acceleration at  $z = 0.05$  m.

Parts a and b of Figure 17 show that the local  $h_q$  and  $h_m$  change with  $x$  near the air–desiccant interface ( $y = 0.0035$  m and  $z = 0.05$  m), respectively, where the heat and mass transport is important. As seen in Figure 18, the heat and mass transfer coefficients at the beginning of the bed at  $x = 0.1$  m (leading edge) are relatively large because  $(\partial u/\partial y)$  near the air–desiccant interface is large. The heat and mass transfer coefficients decay as  $x$  increases, in accord with the change of  $(\partial u/\partial y)$ .

Parts a and b of Figure 18 show that the local  $h_q$  and  $h_m$  change with  $z$  near the air–desiccant interface ( $y = 0.0035$  m and  $x = 0.105$  m), respectively. Both  $h_q$  and  $h_m$  at the beginning of the bed width at  $z = 0.05$  m are slightly larger because  $(\partial u/\partial y)$  near the air–desiccant interface is large.  $h_q$  and  $h_m$  decay

as  $z$  decreases toward the corner region, in accord with the change of  $(\partial u/\partial y)$ .

Figures 15 and 16 depict that the water content and the water adsorption rate also have the same trend as the heat and mass transfer coefficients shown in Figures 17 and 18. Following boundary layer behavior, the  $u$  velocity gradient in the  $y$ -direction ( $\partial u/\partial y$ ) on the desiccant bed surface is large near the leading edge, and then it decays with  $x$  as the thickness of the boundary layer increases. As a result, the heat and mass fluxes on the desiccant bed surface follow the velocity gradient behavior. This is because the heat and mass fluxes are related to the  $u$  velocity gradient in the  $y$ -direction ( $\partial u/\partial y$ ) through the temperature and concentration gradients in the  $y$ -direction using the scale analysis of the momentum, energy, and mass equations.<sup>10</sup> The water concentration at the desiccant surface follows the mass flux behavior, which is large near the leading edge and decays with  $x$ . Therefore, according to both the direct relationship between the water concentration and the water adsorption rate represented in eq 9 and the local equilibrium relation,  $[W = f(C, T)$ , (eqs 11–13)], the water content and the water adsorption rate resemble the water concentration behavior

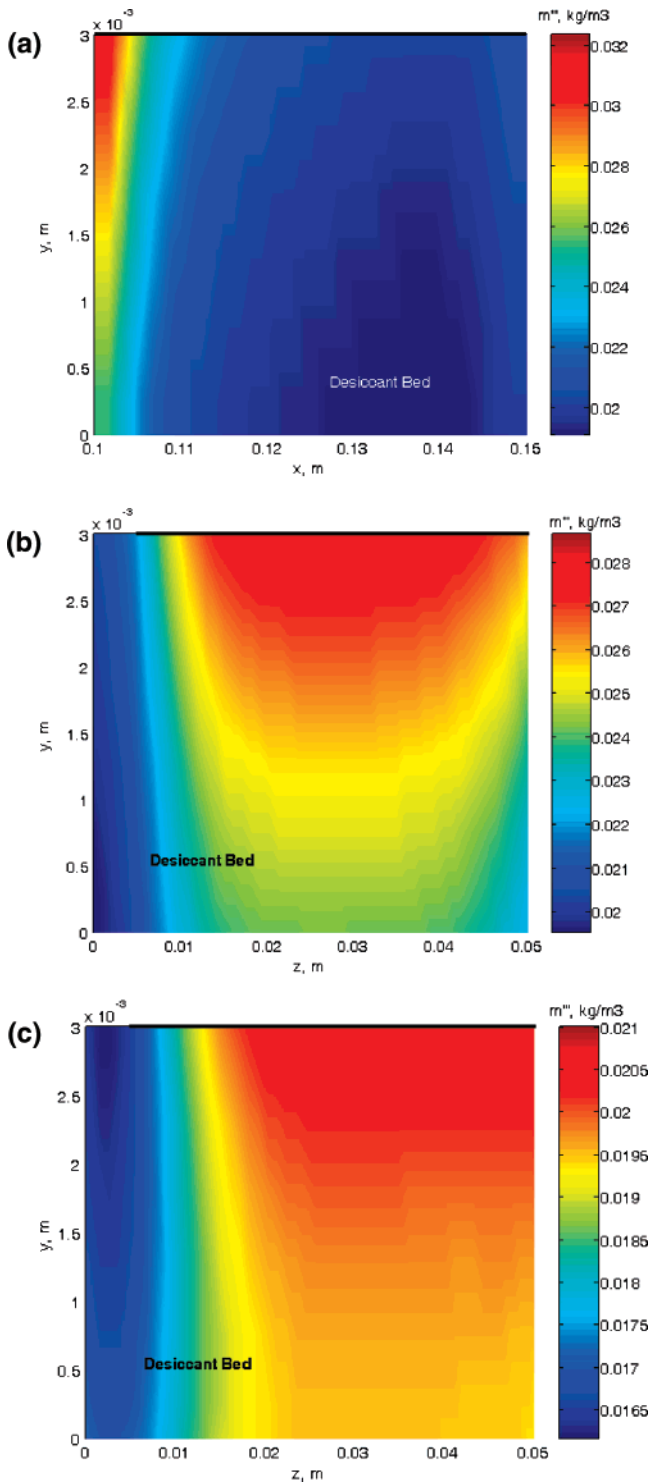


**Figure 14.** Water adsorption rate  $m'''$  for square duct at different cross sections along  $x$ -axis and  $z$ -axis,  $u_\infty = 0.1$  m/s,  $Re = 666$  (square),  $T_\infty = 30$  °C,  $C_\infty = 0.0276$  kg/kg,  $C_w = 0.0075$  kg/kg,  $W_o = 0.1$  kg/kg,  $t = 3$  s,  $b = 0.00321$  m,  $L = 0.05$  m,  $h_\square = 0.1$  m,  $\omega = 0.1$  m,  $P_{ref} = 1.43 \times 10^{-4}$  Pa: (a) A–A cross section at ( $x$ ,  $0 \leq y \leq 0.003$ ,  $z/\omega = 0.5$ ), (b) D–D cross section at ( $x/L = 2.1$ ,  $0 \leq y \leq 0.003$ ,  $z$ ), (c) J–J cross section at ( $x/L = 3$ ,  $0 \leq y \leq 0.003$ ,  $z$ ).

in which they both have the same trend as shown in Figures 15 and 16. Also, since the convective heat and mass coefficients are directly related to the heat and mass fluxes, they follow their behavior in which they both have the same trend as shown in Figures 17 and 18.

Table 2 presents the surface averages of  $(\partial u/\partial y)$ ,  $h_q$ ,  $h_m$ , and  $\Delta p$  for the three duct geometries. The comparison between these

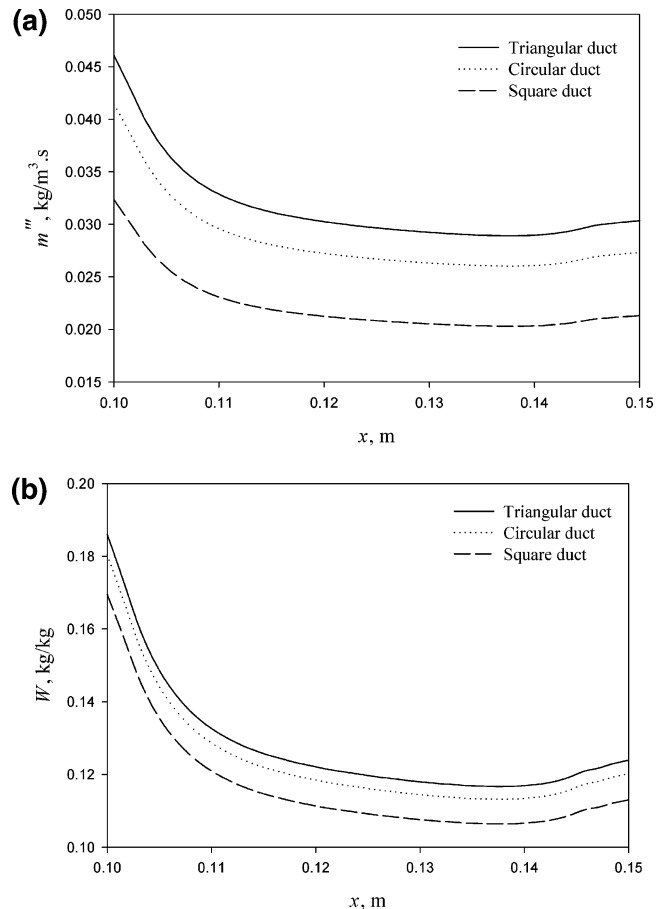


**Figure 15.** Water (a) adsorption rate and (b) content as a function of  $x$  for three duct cross-sectional shapes,  $u_\infty = 0.1$  m/s,  $Re = 666$  (square),  $Re = 466$  (triangular),  $Re = 846$  (circular),  $T_\infty = 30$  °C,  $C_\infty = 0.0276$  kg/kg,  $C_w = 0.0075$  kg/kg,  $W_o = 0.1$  kg/kg,  $t = 3$  s,  $b = 0.00321$  m,  $z = 0.05$  m,  $L = 0.05$  m,  $h_\Delta = 0.141$  m,  $h_\square = 0.127$  m,  $h_\square = 0.1$  m,  $\omega = 0.1$  m,  $P_{ref} = 1.43 \times 10^{-4}$  Pa.

three ducts is performed based on the same inlet air flow velocity and desiccant surface area. The average velocity gradient  $(\partial u/\partial y)_{ave}$  in the circular duct is 12.5% larger than that in the square duct, causing the convective heat and mass transfer coefficients to be also larger by 14%, as shown in Figures 17 and 18. The average  $(\partial u/\partial y)_{ave}$  in the circular duct is 6.6% smaller than that in the triangular duct, which causes the convective heat and mass transfer coefficients to be also smaller by 8.2%, as shown in Figures 17 and 18. The average pressure drop,  $\Delta p_{ave}$ , for the triangular duct is 69% and 73.5% larger than the ones for the square and circular ducts, respectively.

For the desorption process, parts a–d of Figure 19 show the time dependence of the desiccant surface water concentration and surface temperature at  $x = 0.11$  m ( $0.2L$  from the leading edge of the plate),  $y = b$ ,  $z = 0.05$  m ( $z/\omega = 0.5$ ), as well as the overall average water contents and desorption rates for three duct geometries. As expected, and in analogy with the adsorption results, all of these quantities decrease more rapidly at first and then decrease at a slower rate as the bed becomes decreasingly water-laden and, thus, cannot release vapor as rapidly. The temperature and concentration drop to lower values after 0.1 s, which indicates that the extremely rapid desorption by the desiccant occurs within 0.1 s. The physical cause of the drop is similar to that in the adsorption process, which was discussed earlier. In the short time (0–0.1 s) intervals, an initial drop in the water desorption rate occurs because of the rapid drop in the water content. The desorption rate then grows rapidly and becomes asymptotic as the time increases because of the slow

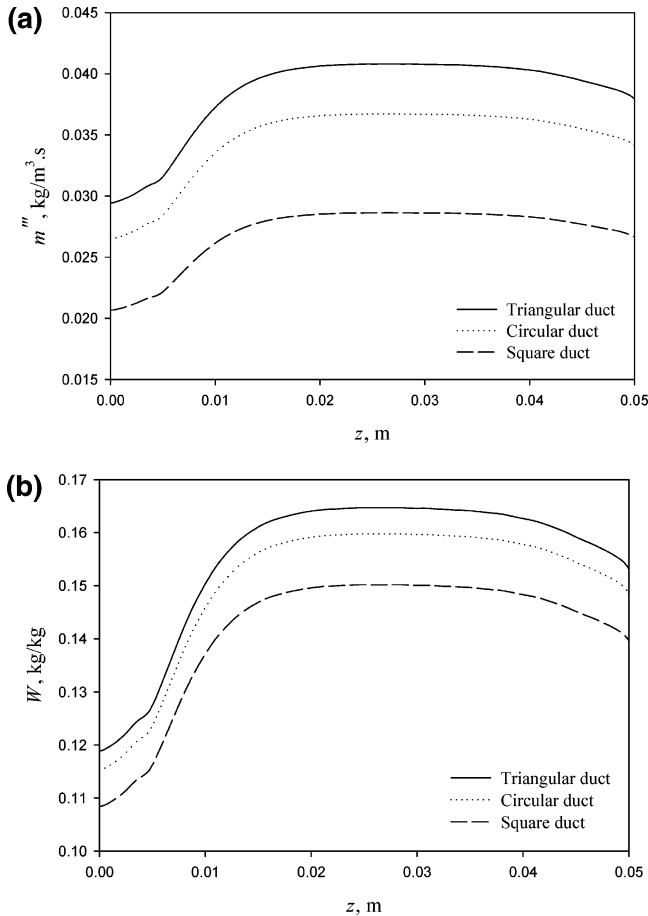


**Figure 16.** Water (a) adsorption rate and (b) content as a function of  $z$  for three duct cross-sectional shapes,  $u_\infty = 0.1$  m/s,  $Re = 666$  (square),  $Re = 466$  (triangular),  $Re = 846$  (circular),  $T_\infty = 30$  °C,  $C_\infty = 0.0276$  kg/kg,  $C_w = 0.0075$  kg/kg,  $W_o = 0.1$  kg/kg,  $t = 3$  s,  $b = 0.00321$  m,  $x = 0.105$  m,  $L = 0.05$  m,  $h_\Delta = 0.141$  m,  $h_O = 0.127$  m,  $h_\square = 0.1$  m,  $\omega = 0.1$  m,  $P_{ref} = 1.43 \times 10^{-4}$  Pa.

decrease in the water content. The magnitudes of the surface water concentration, surface temperature, and the overall average water contents and desorption rates for the circular duct at  $t = 3$  s are 0.05%, 0.066 °C, 5.3%, and 21.9% smaller than those for square duct, and 0.6%, 0.052 °C, 2.3%, and 9.8% larger than those for the triangular duct, respectively. This is due to the duct cross section geometry related changes in the mass transport coefficient, resulting from the change in the  $(\partial u/\partial y)$  near the desiccant bed at  $x = 0.11$  m and  $z = 0.05$  m.

In general, dehumidification effectiveness increases as the flow rate through a desiccant-lined channel is raised, because higher velocities result in a higher convective mass transfer coefficient. Higher velocities increase, however, the flow pressure drop, which also depends importantly on the cross section geometry of the channel, and hence, they also increase the fan work that needs to be invested. The major energy input in desiccation is heat, and the fan work represents the electric energy input. For comparison of the practical utility of the different duct cross section geometries, we evaluate this fan work in a normalized way by defining an electric power consumption figure of merit for the desiccant duct as the work ratio ( $W_r$ ), which is the ratio of the required fan work ( $W_{fan}$ ) (and, thus, accounts for the flow pressure drop) and the work ( $W_{Dehum}$ ) that would have been needed for the amount of dehumidification obtained by desiccant, if it was performed by a vapor compression chiller with a given COP (and, thus, this

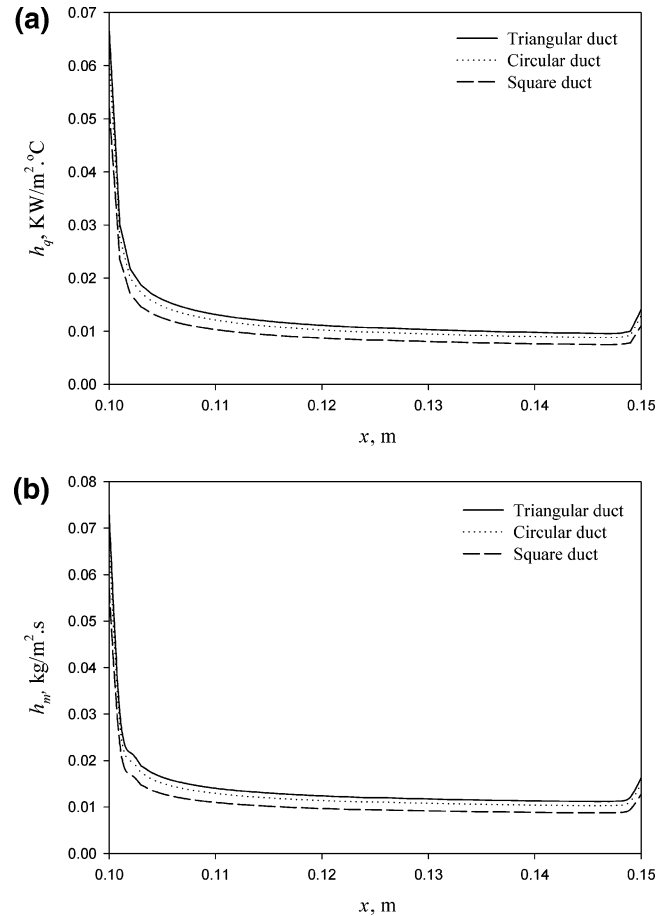


**Figure 17.** Convective (a) heat and (b) mass transfer coefficients as a function of  $x$  for three duct cross-sectional shapes,  $u_\infty = 0.1$  m/s,  $Re = 666$  (square),  $Re = 466$  (triangular),  $Re = 846$  (circular),  $T_\infty = 30$  °C,  $C_\infty = 0.0276$  kg/kg,  $C_w = 0.0075$  kg/kg,  $W_o = 0.1$  kg/kg,  $t = 3$  s,  $b = 0.00321$  m,  $z = 0.05$  m,  $L = 0.05$  m,  $h_\Delta = 0.141$  m,  $h_O = 0.127$  m,  $h_\square = 0.1$  m,  $\omega = 0.1$  m,  $P_{ref} = 1.43 \times 10^{-4}$  Pa.

denominator of  $W_r$  accounts for the dehumidification capacity). This work ratio is, thus, expressed as

$$W_r = \frac{W_{fan}}{W_{Dehum}} = \frac{\bar{u}A_c\Delta p_{ave}/\eta_{Fan}}{mH_f/COP} \quad (54)$$

Other normalizing parameters instead of the vapor compression chiller power demand could be used here, but this one is useful for heating, ventilation, and air conditioning (HVAC) engineers examining common dehumidification options. Using this figure of merit, a lower value of  $W_r$  indicates a better desiccant duct.

Table 3 presents the data used in computing the  $W_r$ , and the computed values of  $W_r$  for the three duct geometries. The results show that  $W_r$  for the triangular duct is 24% and 50.8% larger than the ones for the square and circular ducts, respectively. The fan work for the triangular duct is 46% and 54.5% larger than the ones for the square and circular ducts, respectively. The achieved dehumidification work for the triangular duct is 29.3% and 7.8% larger than the ones for the square and circular ducts, respectively.

According to these results and using  $W_r$  as the figure of merit, the circular duct provides the best dehumidification performance compared with the others. At the same time, it is noteworthy that the triangular duct has the best dehumidification performance as measured by  $m$  and  $W_{Dehum}$  for the same desiccant surface area, but it has the lower  $W_r$  because it creates a larger flow pressure drop. An argument in favor of the triangular cross

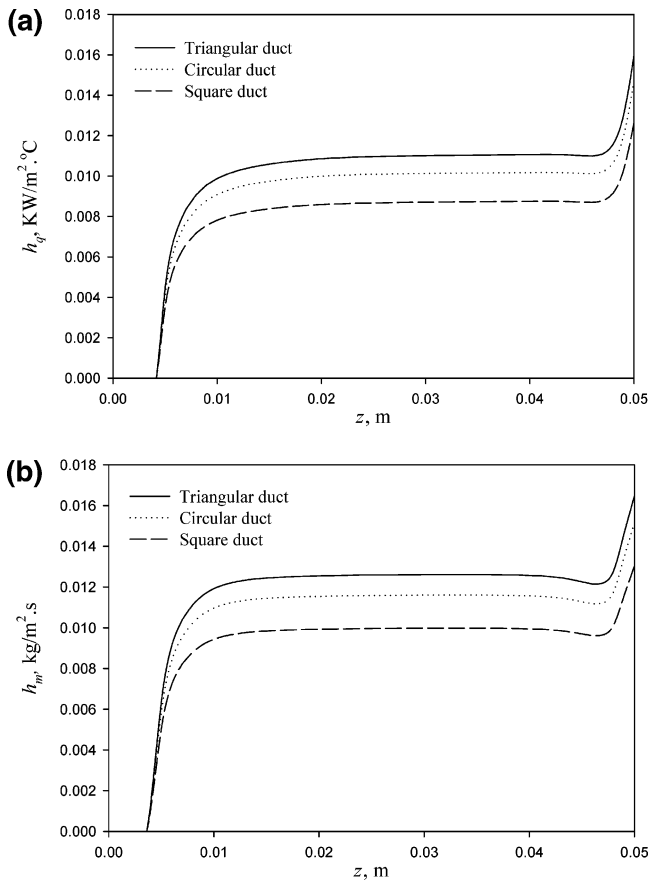


**Figure 18.** Convective (a) heat and (b) mass transfer coefficients as a function of  $z$  for three duct cross-sectional shapes,  $u_\infty = 0.1$  m/s,  $Re = 666$  (square),  $Re = 466$  (triangular),  $Re = 846$  (circular),  $T_\infty = 30$  °C,  $C_\infty = 0.0276$  kg/kg,  $C_w = 0.0075$  kg/kg,  $W_o = 0.1$  kg/kg,  $t = 3$  s,  $b = 0.00321$  m,  $x = 0.105$  m,  $L = 0.05$  m,  $h_\Delta = 0.141$  m,  $h_O = 0.127$  m,  $h_\square = 0.1$  m,  $\omega = 0.1$  m,  $P_{ref} = 1.43 \times 10^{-4}$  Pa.

**Table 3.** Data That Were Used in Computing the Work Ratio  $W_r$  and the Values of  $W_r$  for the Three Ducts; The Conditions Were to Maintain the Same Inlet Air Flow Velocity and Desiccant Surface Area for All Three Ducts<sup>a</sup>

variables	triangular duct	square duct	circular duct
$D_h$ , m	0.07	0.1	0.127
$\bar{u}$ , m/s	0.097	0.117	0.0921
$Re$	466	666	846
$A_c$ , m <sup>2</sup>	0.007	0.01	0.0127
$Q$ , m <sup>3</sup> /s	$0.68 \times 10^{-3}$	$1.17 \times 10^{-3}$	$1.17 \times 10^{-3}$
$\Delta p_{ave}$ , Pa	$3.47 \times 10^{-3}$	$1.08 \times 10^{-3}$	$0.92 \times 10^{-3}$
$m'''$ , kg/m <sup>3</sup> ·s	1.53	1.08	1.38
$m$ , kg/s	$9.2 \times 10^{-5}$	$6.5 \times 10^{-5}$	$8.26 \times 10^{-5}$
$W_{fan}$ , J/s	$2.77 \times 10^{-6}$	$1.49 \times 10^{-6}$	$1.26 \times 10^{-6}$
$W_{Dehum}$ , J/s	33.5	23.68	30.9
$W_r$	$8.27 \times 10^{-8}$	$6.29 \times 10^{-8}$	$4.07 \times 10^{-8}$

<sup>a</sup>  $u_\infty = 0.1$  m/s,  $T_\infty = 30$  °C,  $C_\infty = 0.0276$  kg/kg,  $C_w = 0.0075$  kg/kg,  $W_o = 0.1$  kg/kg,  $t = 3$  s,  $b = 0.00321$  m,  $L = 0.05$  m,  $h_\Delta = 0.141$  m,  $h_O = 0.127$  m,  $h_\square = 0.1$  m,  $\omega = 0.1$  m,  $P_{ref} = 1.43 \times 10^{-4}$  Pa,  $A_s = 0.02$  m<sup>2</sup>,  $\eta_{fan} = 0.85$ ; COP = 7;  $H_1 = 255 \times 10^{-4}$  J/kg;  $V_b = 6 \times 10^{-5}$  m<sup>3</sup>.

section relative to the circular one is that it allows the inclusion of more such ducts in a given cross-sectional area, of, say, a desiccant wheel, than when circular ducts are used, and it also makes it possible to use a shorter duct (thinner wheel) for the same amount of water adsorbed,  $m$ , which would, thus, also proportionally reduce the pressure drop.

## 6. Summary and Conclusions

A transient three-dimensional conjugate model of flow and heat and mass transport for laminar humid air flow in ducts

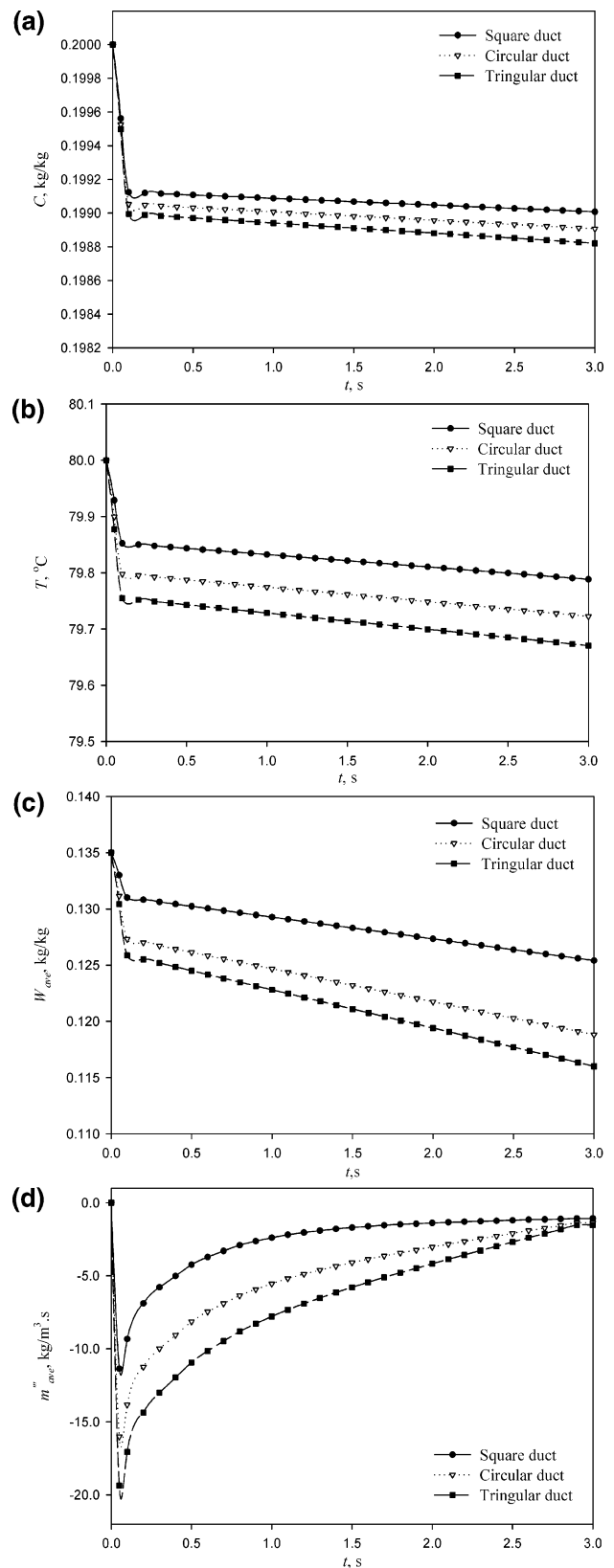


**Figure 19.** Time dependence of the desiccant surface ( $y = b$ ) (a) water concentration ( $x = 0.11$  m and  $z = 0.05$  m), (b) temperature ( $x = 0.11$  m and  $z = 0.05$  m), (c) overall average water content, and (d) overall average water desorption rate for three duct cross-sectional shapes,  $u_\infty = 0.1$  m/s,  $Re = 666$  (square),  $Re = 466$  (triangular),  $Re = 846$  (circular),  $T_\infty = 80$  °C,  $C_\infty = 0.015$  kg/kg,  $C_w = 0.2$  kg/kg,  $W_o = 0.135$  kg/kg,  $t = 3$  s,  $b = 0.00321$  m,  $L = 0.05$  m,  $h_\Delta = 0.141$  m,  $h_O = 0.127$  m,  $h_\square = 0.1$  m,  $\omega = 0.1$  m,  $P_{ref} = 1.43 \times 10^{-4}$  Pa.

with different geometries (triangular, circular, and square) was successfully formulated, solved, and validated. Detailed information about the flow, pressure, temperature, and concentration fields, as well as about the associated heat and mass transfer coefficients, surface concentrations, desiccant water contents, and adsorption rates, was gained and presented. The adsorption/desorption rates for the three duct geometries, as well as the other parameters, increase/decrease rapidly at first, because of the high desiccant interface velocity gradients at the channel entry, and then they increase/decrease at a slower rate because of the gradual diminution of these gradients and because the bed becomes increasingly/decreasingly water-laden and, thus, cannot take up/release vapor as rapidly. The rapid adsorption/desorption by the desiccant occurs within the first 0.1 s; this information allows design optimization of channel length.

Using the figure of merit  $W_r$  that we defined, which is the ratio of the required fan work to the dehumidification attained, the circular duct was found to be the best and the triangular duct was found to be the worst among the three geometries compared, for a given desiccant surface area. At the same time, the triangular duct dehumidifies the most and has some practical advantages when used in systems such as desiccant wheels. Besides the detailed transient 3-D information about the dehumidification rate, concentration, and temperature fields that improve basic process understanding, the results obtained from this study can be useful for designing desiccant ducts, as they give guidance about duct length optimization and duct cross-sectional shape considering both dehumidification effectiveness and flow pressure drop.

## Nomenclature

$A_c$  = cross-sectional flow area,  $m^2$   
 $A_s$  = total desiccant surface area,  $m^2$   
 $b$  = thickness of silica gel bed, m  
 $c$  = specific heat,  $kJ/(kg\ K)$   
 $c_{pa}$  = specific heat of air,  $kJ/(kg\ K)$   
 $c_{pv}$  = specific heat of vapor,  $kJ/(kg\ K)$   
 $C$  = water vapor concentration,  $(kg\ water)/(kg\ mixture)$   
COP = coefficient of performance of chiller  
 $D$  = water vapor diffusivity in air,  $m^2/s$   
 $D_h$  = hydraulic diameter  $(=4A_c/P)$ , m  
 $h$  = overall duct height in the  $y$ -direction, m  
 $h_q$  = heat transfer coefficient,  $kW/m^2\cdot^{\circ}C$ , [ $h_q = q/(T - T_{\infty})$ ]  
 $h_m$  = mass transfer conductance,  $kg/m^2\cdot s$ , [ $h_m = j/(C - C_{\infty})$ ]  
 $H_1$  = adsorption heat,  $kJ/kg$  of water vapor  
 $j$  = mass flux,  $kg/m^2\cdot s$   
 $k$  = heat conductivity,  $kW/(m\cdot K)$   
 $L$  = length of silica gel bed in the  $x$ -direction, m  
 $m$  = amount of water adsorbed by the duct,  $kg_w/s$ , [ $m = (m''' \times V_b)$ ]  
 $m'''$  = water absorption rate into silica gel,  $(kg\ of\ water\ vapor)/(s\ m^3)$   
 $p_r$  = relative pressure, Pa  
 $p_g$  = gauge pressure, Pa  
 $P$  = duct perimeter, m  
 $Re$  = Reynolds number, [ $uD_h/\nu$ ]  
 $q$  = heat flux,  $kW/m^2$   
 $Q$  = volumetric flow rate,  $m^3/s$ , [ $Q = \bar{u} \times A_c$ ]  
 $u$  =  $x$  component of velocity,  $m/s$   
 $\bar{u}$  = average velocity in duct,  $m/s$   
 $T$  = temperature,  $^{\circ}C$   
 $t$  = time, s  
 $V_b$  = total desiccant bed volume,  $m^3$   
 $v$  =  $y$  component of velocity,  $m/s$

$W$  = water content,  $(kg\ of\ water\ vapor)/(kg\ of\ desiccant)$

$W_r$  = work ratio

$W_{fan}$  = fan work,  $J/s$

$W_{Dehum}$  = dehumidification work,  $J/s$

$w$  =  $z$  component of velocity,  $m/s$

## Greek Symbols

$\alpha$  = thermal diffusivity,  $m^2/s$

$\Delta p_{ave}$  = average pressure drop in the duct (eq 18), Pa

$\eta_{fan}$  = fan efficiency

$\phi$  = relative humidity in bulk stream,  $(kg\ of\ vapor)/(kg\ of\ air)$

$\nu$  = kinematics viscosity,  $m^2/s$

$\rho$  = density,  $kg/m^3$

$\sigma$  = porosity

$\omega$  = overall duct width in the  $z$ -direction, m

## Subscripts

ave = average

b = desiccant bed

f = fluid (i.e., air)

s = solid desiccant

w = wall, i.e., the silica gel bed

$\infty$  = free stream conditions

$\Delta$  = triangular

$\square$  = square

$\circ$  = circular

## Literature Cited

- (1) Fujii, Y.; Lior, N. Conjugate Heat and Mass Transfer in a Desiccant-Airflow System: A Numerical Solution Method. *Numer. Heat Transfer* **1996**, *29*, 689.
- (2) Al-Sharqawi, H.; Lior, N. Conjugate Computation of Transient Flow and Heat and Mass Transfer Between Humid Air and Desiccant Plated and Channels. *Numer. Heat Transfer* **2004**, *46*, 525.
- (3) Niu, J.; Zhang, L. Effects of Wall Thickness on the Heat and Moisture Transfers in Desiccant Wheels for Air Dehumidification and Enthalpy Recovery. *Int. Commun. Heat Mass Transfer* **2002**, *29* (2), 255.
- (4) Niu, J.; Zhang, L. Heat Transfer and Friction Coefficient in Corrugated Ducts Confined by Sinusoidal and Arc Curves. *Int. J. Heat Mass Transfer* **2002**, *45*, 571.
- (5) Haji-Sheikh, A.; Vafai, K. Analysis of Flow and Heat Transfer in Porous Media Impeded Inside Various-Shaped Ducts. *Int. J. Heat Mass Transfer* **2004**, *47*, 1889.
- (6) Haji-Sheikh, A. Fully Developed Heat Transfer to Fluid Flow in Rectangular Passages Filled With Porous Materials. *Trans. ASME* **2006**, *128*, 550.
- (7) Hooman, K.; Gurgenci, H.; Merrikh, A. Heat Transfer and Entropy Generation Optimization of Forced Convection in Porous-Saturated Ducts of Rectangular Cross-Section. *Int. J. Heat Mass Transfer* **2007**, *50*, 2051.
- (8) Mei, V. C.; Lavan, Z. Performance of Cross-Cooled Desiccant Dehumidifiers. *ASME J. Solar Energy Eng.* **1983**, *105*, 300.
- (9) Patankar, S. V. *Numerical Heat and Fluid Flow*; Taylor & Francis: New York, 1980.
- (10) Al-Sharqawi, H. S. A Conjugate Transient Computational Analysis of Flow, Heat, and Mass Transfer in Desiccant-Airflow Systems. Ph.D. Dissertation, University of Pennsylvania, Philadelphia, PA, 2002.
- (11) Burmeister, L. C. *Convective Heat Transfer*; Wiley: New York, 1993.
- (12) Pesaran, A. A.; Mills, A. F. Moisture Transport in Silica Gel Packed Beds. I. Theoretical Study. *Int. J. Heat Mass Transfer* **1987**, *30*, 1037.
- (13) Pesaran, A. A.; Mills, A. F. Moisture Transport in Silica Gel Packed Beds. II. Experimental Study. *Int. J. Heat Mass Transfer* **1987**, *30*, 1051.
- (14) Fang, F.; Chen, J.; Hong, Y. Experimental and Analytical Evaluation of Flow in a Square-to-Square Wind Tunnel Contraction. *J. Wind Eng. Ind. Aerodynamics* **2001**, *89*, 247.

Received for review May 23, 2007

Revised manuscript received November 26, 2007

Accepted December 4, 2007